



1 **Retrieval of aerosols over Asia from the Advanced Himawari Imager: Expansion of**  
2 **temporal coverage of the global Dark Target aerosol product**

3  
4 Pawan Gupta<sup>1,2</sup>, Robert C. Levy<sup>2</sup>, Shana Mattoo<sup>2,3</sup>, Lorraine A. Remer<sup>4</sup>, Robert E. Holz<sup>5</sup>,  
5 Andrew K. Heidinger<sup>6</sup>

6  
7 [1] {STI, Universities Space Research Association (USRA), Huntsville, AL, USA}

8 [2] {NASA Goddard Space Flight Center, Greenbelt, MD 20771, USA}

9 [3] {Science Systems and Applications, Inc, Lanham, MD 20709, USA}

10 [4] {JCET, University of Maryland – Baltimore County, Baltimore, MD 21228, USA}

11 [5] {SSEC, University of Wisconsin-Madison, WI 53707, USA}

12 [6] {NOAA Advanced Satellite Product Branch, Madison, WI 53707, USA}

13

14 Correspondence to: Pawan Gupta ([pawan.gupta@nasa.gov](mailto:pawan.gupta@nasa.gov))

15

16 **Abstract**

17

18 For nearly two decades we have been quantitatively observing the Earth’s aerosol system  
19 from space at one or two times of the day by applying the Dark Target family of  
20 algorithms to polar-orbiting satellite sensors, particularly MODIS and VIIRS. With the  
21 launch of the Advanced Himawari Imager (AHI) and the Advanced Baseline Imagers  
22 (ABIs) into geosynchronous orbits, we have the new ability to expand temporal coverage  
23 of the traditional aerosol optical depth (AOD) to resolve the diurnal signature of aerosol  
24 loading during daylight hours. Here, we describe how the Dark Target aerosol  
25 algorithms are adopted for the wavelengths and resolutions of AHI, and show retrieval  
26 results from AHI for a two-month period of May-June 2016. The AHI-retrieved AOD is  
27 collocated in time and space with existing AEROSOL ROBOTIC NETWORK stations across  
28 Asia and with collocated Terra- and Aqua-MODIS retrievals. The new AHI AOD



29 product matches AERONET, as well as does the standard MODIS product, and the  
30 agreement between AHI and MODIS retrieved AOD is excellent, as can be expected by  
31 maintaining consistency in algorithm architecture and most algorithm assumptions.  
32 Furthermore, we show that the new product approximates the AERONET-observed  
33 diurnal signature. Examining the diurnal patterns of the new AHI AOD product we find  
34 specific areas over land where the diurnal signal is spatially cohesive. For example, in  
35 Bangladesh the AOD increases by 0.50 from morning to evening, and in northeast China  
36 the AOD decreases by 0.25. However, over open ocean the observed diurnal cycle is  
37 driven by two artifacts, one associated with solar zenith angles greater than 70° that may  
38 be caused by a radiative transfer model that does not properly represent spherical Earth,  
39 and the other artifact associated with the fringes of the 40° glint angle mask. Future work  
40 to make the Dark Target AHI algorithm operational will need to re-examine masking  
41 including snow mask, re-evaluate assumed aerosol models for geosynchronous geometry,  
42 address the artifacts over the ocean and investigate size parameter retrieval from the over  
43 ocean algorithm.

44

45

## 46 **1.0 Introduction**

47

48 Atmospheric aerosols, small liquid or solid particles suspended in the atmosphere, play a  
49 key role in Earth's energy balance, cloud physics, geochemical cycles and air  
50 quality/public health (Boucher et al., 2013; Rosenfeld et al., 2014ab; Seinfeld et al., 2016;  
51 Jickells et al., 2005; Yu et al., 2015; Lim et al., 2012). These particles originate from  
52 both human activity and natural processes, and they can cover vast regions of the globe.  
53 Observations from satellite sensors provide the best means for monitoring and  
54 quantifying the extent and transport of large-scale aerosol events (Kaufman et al., 2005;  
55 Yu et al., 2012), and provide some characterization of aerosol particle properties (Remer  
56 et al., 2005; Torres et al., 2013; Kalashnikova and Kahn, 2006; Kahn and Gaitley 2015).  
57 Especially since the launch of NASA's Earth Observing System (EOS) and similar  
58 satellites by international agencies, the community has benefitted from nearly two  
59 decades of quantitative measures of the global aerosol system. While both passive and



60 active sensors have contributed to our understanding of the global aerosol system, here  
61 we focus on only passive sensors. These, such as the MODerate resolution Imaging  
62 Spectroradiometer (MODIS) (Levy et al., 2013; Hsu et al. 2013; Lyapustin et al., 2011),  
63 the Multiangle Imaging Spectro-Radiometer (MISR) (Diner et al., 1998; Martonchik  
64 1998; Kahn et al., 2010), the Ozone Monitoring Instrument (OMI) (Torres et al., 2013),  
65 and POLarization and Directionality of the Earth's Reflectances (POLDER) (Tanré et al.,  
66 2011) have provided instantaneous measures of aerosol loading, particle size, particle  
67 absorption and aerosol type across the globe. The community has used these data to  
68 calculate decadal statistics of aerosol climatology, seasonal and monthly statistics,  
69 quantitative measures of intercontinental aerosol transport and fertilization of ecosystems  
70 (Remer et al., 2008; Yu et al., 2012, 2013, 2015). These satellite aerosol products have  
71 been used to estimate aerosol radiative effects and climate forcing, associations between  
72 aerosols and cloud micro- and macrophysics, precipitation, air quality and public health,  
73 and have provided critical constraints on global climate modeling (Zhang et al., 2005;  
74 Koren et al. 2005; Lin et al. 2006; Wang and Christopher, 2003; Quaas et al., 2009;  
75 Patadia et al., 2008; to give just one early example of each application).

76  
77 The sensors mentioned above all have been launched on polar orbiting satellites in low  
78 earth orbit (LEO). Such satellites are sun synchronous, passing over each location on  
79 Earth at approximately the same local solar time each day. A LEO sensor imaging a  
80 broad swath of Earth will image every spot on Earth, and thus achieve full global  
81 coverage in 1 or 2 days. However, each spot on Earth is only viewed once per day in  
82 daylight and once per day at night, always at approximately the same local solar time. In  
83 contrast a geosynchronous (GEO) satellite orbits at a high altitude above Earth, matching  
84 the same period as the Earth's rotation. A sensor on a GEO satellite can scan the full or  
85 partial portion of Earth's face presenting to the satellite. Neither the sensor nor the Earth  
86 appear to move in these images although the terminator between day and night on the  
87 Earth appears to move from east to west across the image over time. A GEO imager  
88 always views the same Earth locations across approximately 1/3 of the Earth, and cannot  
89 by itself provide full global coverage. However, a sensor on a GEO satellite can provide



90 information on the aerosol in any viewed location as a function of time of the day,  
91 enabling monitoring of the diurnal cycle.  
92  
93 For about a decade there has been a publicly available operational aerosol product  
94 derived from a GEO sensor. This is the GOES Aerosol Smoke Product (GASP) (Prados  
95 et al., 2007), where GOES stands for Geostationary Operational Environmental Satellite.  
96 GASP provides aerosol optical depth for the daylight section of the continental United  
97 States at 4 km spatial resolution every 30 minutes in near real time, and the data is  
98 archived. The sensor has only five channels, one spectrally broad channel (0.52–0.71  $\mu\text{m}$ )  
99 in the visible and four in the near to thermal infrared. The aerosol retrieval algorithm  
100 makes use of the infrared channels for cloud masking, but must acquire all of its aerosol  
101 information from a single visible channel. The lack of a channel in the shortwave  
102 infrared (e.g. 2.1 or 2.2  $\mu\text{m}$ ) prohibits application of an EOS-era Dark Target retrieval  
103 (Kaufman et al., 1997; Levy et al., 2007) and the lack of any channel in the blue  
104 eliminates the possibility of a Deep Blue retrieval (Hsu et al. 2004, 2013). Thus the  
105 GASP retrieval is handicapped by the relative primitiveness of the GOES-13 sensor.  
106 Even so, aerosol optical depth (AOD) retrievals from GASP collocated and compared  
107 with AOD measurements from the AERosol Robotic NETwork (AERONET; Holben et  
108 al. 1998) at 10 sites in the northeastern U.S. and Canada showed reasonable agreement.  
109 Regression of GASP and AERONET AOD derived correlation of 0.79, rms difference of  
110 0.13, and absolute bias of less than 30% for larger AOD (e.g. AOD > 0.1). Validation in  
111 the southeast and western U.S. was less good. The GASP validation statistics are  
112 reasonable, but not as good as those produced by MODIS AOD retrievals at the same  
113 AERONET locations. The main point of GASP, though, is not its absolute accuracy, but  
114 that it provides quantitative information on the diurnal cycle of aerosol across the  
115 continental United States and southern Canada.  
116  
117 We are now entering a new era in GEO observations. With the launch of the Advanced  
118 Himawari Imager (AHI) in (Yu and Wu, 2016) and the Advanced Baseline Imager (ABI)  
119 on GOES-16 and GOES-17 (Kalluri et al., 2018), we have sensors in GEO orbit with  
120 spectral capability similar to MODIS. AHI has 16 bands, including three in the visible



121 and another in the SWIR. ABI also has 16 bands, but distributed differently across the  
122 visible to the SWIR. This spectral capability combined with nominal spatial resolution  
123 0.5 to 2 km creates opportunity for aerosol retrievals that can advance beyond what  
124 GASP could produce. Aerosol algorithms developed and implemented by the agencies  
125 responsible for the operations of the GEO satellites are or will be produced operationally  
126 and made public. These include the Japanese Meteorological Agency (JMA) for AHI on  
127 Himawari (Uesawa, 2016) and the National Oceanographic and Atmospheric Agency  
128 (NOAA) for ABI on the GOES-R series. In addition to these official operational  
129 products, other algorithms have been developed that make use of the new generation of  
130 GEO observations for aerosol retrievals, especially for AHI data (Sekiyama et al., 2015;  
131 Yumimoto et al., 2016; Lim et al., 2016, 2018ab; Zhang et al., 2018; Yoshida et al.,  
132 2018; Yang et al., 2018; Shi et al., 2018; Yan et al., 2018). Some of these alternative  
133 aerosol products are research algorithms for specific purposes, while others could be of  
134 general interest and could be made public.

135

136 Because the capabilities of the new GEO sensors replicate the important spectral and  
137 spatial capabilities of the MODIS sensors, the MODIS Dark Target (DT) algorithms over  
138 land and ocean (Remer et al., 2005; Levy et al., 2010, 2015, 2018; Gupta et al., 2016) can  
139 be applied to AHI or ABI observations with only minor adjustments. The expectation is  
140 that the resulting aerosol product will match the original MODIS product in terms of  
141 accuracy and availability (number of retrievals). More than providing just another  
142 alternative aerosol product to the community, application of the traditional DT algorithm  
143 to GEO sensors offers continuity with a nearly 20-year well-studied, validated, and  
144 accepted aerosol product. The continuity of a DT AHI or ABI algorithm means that there  
145 could be an accurate MODIS-like aerosol product that resolves the day time diurnal  
146 cycle, providing a well-understood quantitative measure of aerosol loading at fine  
147 temporal resolution at the large regional scale.

148

149 In this study we present the results of the first attempt at porting the MODIS DT aerosol  
150 algorithm to the AHI sensor on the Himawari-8 geosynchronous satellite. The AHI  
151 inputs and the algorithm will be described in Section 2, with emphasis made on how the



152 AHI algorithm differs compared to the MODIS implementation. Section 3 will present  
153 results and compare these with standard MODIS retrievals and collocated ground-based  
154 observations. Section 4 will explore the AHI aerosol product's diurnal cycle at  
155 AERONET stations for validation, and then question how well the diurnal mean AOD  
156 inferred from once-a-day LEO observations compare with a truer diurnal mean compared  
157 from observations made at finer temporal resolution. Finally, results will be summarized  
158 and discussed in Section 5.

159

## 160 **2.0 Data and retrieval algorithm**

161

### 162 **2.1 AHI sensor characteristics**

163

164 The AHI was first launched on the Himawari-8 satellite in 2014 and became operational  
165 in July 2015. It is in geosynchronous orbit over the equator at 140.7° East. The second  
166 AHI was launched on the Himawari-9 in November 2016 and remains in a standby mode.  
167 The instrument has the capability to image a mesoscale region every 30 seconds while  
168 providing full disk coverage every 10 minutes. In this study use the full disk data. The  
169 data to be presented here were obtained from the University of Wisconsin atmospheric  
170 Science Investigator lead Processing System (SIPS) which processed the NOAA's  
171 operational cloud operating system – extended (CLAVR-x) which provides all 16  
172 channels at a consistent 2km resolution. For this analysis we processed the DT algorithm  
173 at 1-hour temporal resolution from 0000 UTC to 0800 UTC, 9 full disk images per day.  
174 Figure 1 shows an example of the AHI full disk image. AHI wavelengths used in the DT  
175 aerosol retrieval along with their spatial resolution are shown in Table 1, and compared  
176 with their counterparts from the MODIS and Visible InfraRed Imaging Radiometer Suite  
177 (VIIRS) instruments. From Table 1 we see that AHI nearly matches MODIS and VIIRS,  
178 wavelength by wavelength in the bands needed by the DT algorithm, except for missing  
179 the 1.24  $\mu\text{m}$  band that is used in the aerosol retrieval over ocean and also in masking  
180 snow/ice over land and sediments in the ocean. It is also missing the 1.38  $\mu\text{m}$  channel  
181 that the DT aerosol algorithm has relied on for identifying and masking thin cirrus. For  
182 the bands that overlap MODIS, although close in spectral resolution, they do not exactly



183 match. For this reason the algorithm Look Up Tables (LUT), gas absorption corrections  
184 etc. cannot be applied directly from the current MODIS algorithm and must be calculated  
185 specifically for AHI.  
186



187  
188 Figure 1. Full disk true color image from AHI using the 0.64  $\mu\text{m}$ , 0.51  $\mu\text{m}$ , 0.47  $\mu\text{m}$   
189 channels. The image is taken on October 20, 2018 at 02:10 UTC.

190  
191 AHI's spatial resolution is coarser than MODIS's, but comparable to VIIRS. Note,  
192 however, that the spatial resolution noted in Table 1 refers to the subsatellite point. The  
193 spatial resolution of Earth scenes at the edges of MODIS and VIIRS swaths or at the edge  
194 of the AHI disk will have spread from their subsatellite value. MODIS pixels spread by 4  
195 times their nadir value, and VIIRS pixels spread by 2 times. AHI pixels remain 1-3 times  
196 their size at the subsatellite point for all but the extreme edge of the full disk image.



197 Table 1. MODIS, VIIRS and AHI wavelengths in  $\mu\text{m}$  used directly in the DT algorithm  
198 (**bold**) and subsatellite point spatial resolution in kilometers

199

200

201

202

203

204

205

206

207

208

209

MODIS	VIIRS	AHI
<b>0.47</b> /0.5	<b>0.49</b> /0.75	<b>0.47</b> /1.0
<b>0.55</b> /0.5	<b>0.55</b> /0.75	<b>0.51</b> /1.0
<b>0.66</b> /0.25	<b>0.67</b> /0.75	<b>0.64</b> /0.5
<b>0.86</b> /0.25	<b>0.86</b> /0.75	<b>0.86</b> /1.0
<b>1.24</b> /0.5	<b>1.24</b> /0.75	
<b>1.38</b> /0.5	<b>1.38</b> /0.75	
<b>1.61</b> /0.5	<b>1.61</b> /0.75	<b>1.61</b> /2.0
<b>2.11</b> /0.5	<b>2.25</b> /0.75	<b>2.25</b> /2.0

210 Given that the wavelengths and spatial resolution of AHI differ slightly from the heritage  
211 DT aerosol algorithm means that while the structure, heritage and experience of the  
212 MODIS DT algorithm can be adapted for AHI to maintain as much continuity as  
213 possible, the resulting AHI algorithm and product will not be an identical twin.

214

## 215 **2.2 Dark Target AHI aerosol algorithm and research product**

216

217 The DT aerosol algorithms are a family of algorithms, based on the original two  
218 algorithms that retrieved aerosol over ocean and over land from the MODIS instruments  
219 aboard NASA's Terra and Aqua satellites. Levy et al. (2010, 2015, 2018) and the on-line  
220 Algorithm Theoretical Basis Document (<https://darktarget.gsfc.nasa.gov>) describe these  
221 algorithms in depth. Here we only provide an overview in order to highlight the  
222 differences between the original algorithms and the DT algorithm applied to AHI inputs.  
223 DT algorithms should not be confused with other operational NASA aerosol algorithms  
224 applied to MODIS inputs (e.g. Deep Blue; Hsu et al., 2013 and MAIAC: Lyapustin et al.,  
225 2011). Both DT ocean and DT land procedures use Lookup Tables (LUTs). LUTs are  
226 created by using radiative transfer (RT) code to simulate spectral top-of-atmosphere  
227 (TOA) reflectance for expected conditions of aerosols over a theoretical rough ocean



228 surface or black land surface. These LUTs assume intrinsic physical and optical  
229 properties (size, shape, refractive index) as well as total column loading of atmospheric  
230 aerosols.  
231  
232 The original DT retrieval relies on seven reflective solar bands for aerosol retrieval and  
233 one for cirrus detection and masking (Table 1). Additional bands are used for tasks like  
234 cloud masking, snow identification, etc. The algorithm adapted for AHI makes use of 6  
235 bands for the aerosol retrieval that are similar, but not exactly the same as the original  
236 MODIS ones. The differences require new corrections for trace gas absorption in the  
237 channels, and the calculations of new LUTs. It is thus impossible to exactly duplicate the  
238 DT algorithm as it is ported from sensor to sensor. However, the basic physical  
239 assumptions, RT codes, algorithm architecture, and intrinsic physical, and optical  
240 properties used to calculate the LUTs are the same in the AHI DT algorithm, as they are  
241 in the current MODIS and VIIRS DT algorithms.  
242  
243 The greatest consequences to missing the 1.24  $\mu\text{m}$  band is in sediment masking for ocean  
244 and snow/ice masking for land. New techniques that compensate for the missing  
245 information were applied to the AHI data. For sediment masking, we follow Li et al.  
246 (2003) as is standard for the DT algorithm, but substitute the 1.61 channel for the  
247 standard 1.24  $\mu\text{m}$  channel. Physically this substitution should work, as both channels are  
248 expected to be black in sea water, which provides the background from which sediments  
249 are flagged, but the substitution has not yet been well-validated. We have not yet devised a  
250 substitute for the over land snow/ice mask. The data analyzed and shown here are from  
251 May and June 2016, months when no snow is expected in the domain. Devising, testing  
252 and implementing an AHI snow mask will be needed before the DT AHI algorithm can  
253 be applied year round. In terms of the direct aerosol retrieval, the lack of the 1.24  $\mu\text{m}$   
254 information only affects the over ocean algorithm slightly, as the information from the  
255 0.86  $\mu\text{m}$  and the two longer wavelengths compensate for its absence (Tanré et al., 1996;  
256 1997).  
257



258 The loss of the 1.38  $\mu\text{m}$  channel may have more pronounced consequences as it proved to  
259 be the first line of defense against thin cirrus contamination in the aerosol product (Gao  
260 and Kaufman, 1995). In this initial adaptation of the algorithm to AHI we have not  
261 implemented any alternative test for thin cirrus, and therefore cirrus contamination is  
262 expected in the results shown here. For clouds other than thin cirrus, we apply an internal  
263 cloud mask to the input radiances, similar to the traditional MODIS aerosol cloud mask.  
264 This mask is based on spatial variability of groupings of 3x3 input radiance pixels  
265 (Martins et al., 2002). Because of the similar size of the native pixels in AHI to MODIS,  
266 the same thresholds were used. However, while the MODIS aerosol cloud mask also  
267 incorporates specific tests from the standard MODIS cloud mask (MOD/MYD35: Frey et  
268 al. 2008) that are based on thermal infrared channels, those products are not available for  
269 AHI. No direct substitution is employed to compensate. The absence of these specific  
270 external cloud mask tests will mostly affect high cold cloud identification, and again this  
271 suggests that the results shown here will be affected by cirrus contamination. Because  
272 alternative methods have not been developed for masking clouds, and the alternative  
273 method for identifying sediments has not been vetted to the same extent as the original  
274 MODIS DT masking techniques. Therefore, the possibility of contamination from these  
275 features affecting the aerosol retrievals is higher than expectations based on the MODIS  
276 heritage.

277  
278 The AHI retrieval algorithm aggregates 10x10 boxes of native resolution (2 x 2 km)  
279 reflectance data, to create retrieval boxes that have nominal resolution of 20 x 20  
280 km (at the subsatellite point). Different tests (spectral, spatial, etc) perform cloud  
281 masking, sediment masking and glint masking, so that the 10 x 10 box is made up of only  
282 pixels appropriate for aerosol retrieval. There are corrections for gas absorption ( $\text{H}_2\text{O}$ ,  
283  $\text{O}_3$ ,  $\text{CO}_2$ ), along with some statistical filtering. The result is a single set of spectral  
284 reflectances in the six bands that is input to the retrieval algorithm. Additional inputs  
285 include ancillary data such as ozone profiles, wind speed and water vapor columns from  
286 NOAA's Global Data Assimilation System (GDAS) reanalysis data, and a global land/sea  
287 mask generated by CLAVR-x at 2 km resolution.

288



289 Whether ocean or land, the DT retrieval searches the pre-computed LUTs to find the best  
290 match to the spectral observations. This derives the total aerosol loading (AOD) defined  
291 at 0.55  $\mu\text{m}$ , even for AHI that does not have a 0.55  $\mu\text{m}$  channel. This is the primary  
292 wavelength of the retrieval, but AOD at other wavelengths are also reported. Two  
293 measures of aerosol particle size are given for the over ocean retrieval, Fine Mode  
294 Weighting and Ångström Exponent (AE). AHI-retrieved aerosol size parameters will not  
295 be examined in this paper. Although the ocean and land retrievals have similarities, the  
296 details are different because land surface optical properties are different than ocean. The  
297 ocean algorithm calculates a “rough” surface (whitecaps, foam, glitter), which is a  
298 function of wind-speed, while the land algorithm assumes quasi-static ratios between blue  
299 (0.47  $\mu\text{m}$ ), red (0.64  $\mu\text{m}$ ), and shortwave infrared (e.g. 2.25  $\mu\text{m}$ ) wavelengths. Land  
300 surface ratios for the retrievals shown in this study are identical to those used by the  
301 standard MODIS Collection 6.1 algorithm. Ideally these ratios should be re-examined for  
302 the specific AHI wavelengths at a later time. In addition to the aerosol properties, DT  
303 provides many diagnostics including Quality Assurance and Confidence (QAC).

304

305 The new AHI DT algorithm was applied to input AHI full disk radiances, day light  
306 portion of the disk-only. View angles were confined to less than 72 degrees and solar  
307 zenith angles were restricted to less than 80 degrees. The period of interest spans two  
308 months (May-June 2016) and includes the time period of the Korea-U.S. Air Quality  
309 (KORUS-AQ) field experiment in which the ground truth infrastructure within the AHI  
310 disk was greatly expanded. Given 9 images per day, the data base for analysis thus  
311 includes more than 549 disk images of AOD derived from AHI inputs using the new AHI  
312 DT algorithm.

313

### 314 **2.3 MODIS aerosol products**

315

316 The AOD retrieved from AHI using the DT retrieval will be compared with the more  
317 established and well-characterized DT AOD product from MODIS on board the Terra  
318 and Aqua satellites. Specifically we will be accessing Collection 6.1 Level 2 MOD04  
319 and MYD04 data products, where MOD refers to products derived from Terra MODIS



320 inputs and MYD refers to those derived from Aqua MODIS inputs. Level 2 refers to  
321 derived geophysical parameters from the Level 1b geolocated and calibrated measured  
322 radiance inputs. Level 2 data are provided in 5 minute cut sections of the orbital image  
323 called granules. These images are not gridded, but instead follow directly from the  
324 instrument scan as it follows its orbital path. There are many individual aerosol and  
325 diagnostic parameters within each MOD/MYD04 file. This study makes use of only one  
326 parameter, Optical\_Depth\_Land\_And\_Ocean. This parameter combines the retrieved  
327 AOD at  $0.55 \mu\text{m}$  from the independent algorithms applied separately over land and  
328 ocean, and uses only those retrievals identified with the highest quality (QAC=3 over  
329 land and  $\text{QAC} > 0$  over ocean). MODIS granules were selected that fall within the  
330 daylight portion of the AHI radiances, corresponding to the same days of the AHI images  
331 analyzed. Further temporal ( $\pm 0.5$  hour) and spatial ( $0.25 \times 0.25$  degree) collocations have  
332 been performed for specific analysis.

333

#### 334 **2.4 AERONET aerosol products**

335

336 AERONET is a global ground network of CIMEL sun-sky radiometers and data processing  
337 and analysis software commonly used to evaluate satellite-derived aerosol products  
338 (Holben et al., 1998). In this work, only the direct sun measurements will be used.  
339 AERONET processes these spectral measurements to derive AOD at the wavelengths  
340 corresponding to the direct sun measurements. The AERONET spectral AOD product is a  
341 community standard for satellite-derived AOD validation, given that AERONET's AOD  
342 uncertainty of 0.01-0.02 (Eck et al., 1999) is sufficiently more accurate and precise than  
343 can be expected by any satellite retrieval. The configuration of the spectral bands varies,  
344 but typically is centered at 0.34, 0.38, 0.44, 0.50, 0.67, 0.87, and  $1.02 \mu\text{m}$ . Here we use a  
345 quadratic log-log fit (Eck et al., 1999) to interpolate AERONET AOD to  $0.55 \mu\text{m}$  to match  
346 the AHI AOD product. The typical temporal frequency of direct sun measurements is every  
347 15 minutes. The network consists of hundreds of stations, located globally, across all  
348 continents and in a wide variety of aerosol, meteorological and surface type conditions.  
349 Here, we only include stations within the AHI view disk. AOD data from AERONET are  
350 reported for three different quality levels: unscreened (level 1.0), cloud screened (level 1.5)



351 and cloud screened and quality assured (level 2.0). We will only use Version 3 Level 2.0  
352 AERONET AODs in this study.

353

### 354 **3.0 Comparison with AERONET and MODIS DT**

355

356 The new AHI DT algorithm was applied to AHI-measured radiances over the full disk  
357 (except for extreme viewing and solar angles), daily, through the 9 measurement times  
358 (hourly: 0000 to 0800 UTC). We will test this new product by first validating it against  
359 collocated AERONET measurements and then comparing it with the well-vetted MODIS  
360 DT product.

361

### 362 **3.1 Validation against collocated AERONET AOD**

363

364 The validation procedure requires calculating the spatio-temporal statistics of a collocated  
365 AHI-retrieved and AERONET-measured AOD pair (Ichoku et al. 2002; Petrenko et al.,  
366 2012; Munchak et al., 2013; Remer et al., 2012, Gupta et al., 2018). Thus, the temporal  
367 mean AOD of all AERONET AOD measurements within  $\pm 30$  minutes of an AHI scan will  
368 be compared with the spatial mean of all AHI-retrieved AOD values within a  $0.25 \times 0.25$   
369 degree box around the AERONET station. From the collection of these ordered pairs a set  
370 of correlation and regression statistics will be calculated, assuming that the AERONET  
371 AODs are the independent variables and the AHI AODs are the dependent variables. These  
372 include number of AOD pairs (N), the correlation coefficient (R), the slope (m) and  
373 intercept (I) of the linear regression through the points, the overall mean bias and Root  
374 Mean Square Error (RMSE) of the AHI AODs. Also we apply the expected error (EE),  
375 based on previous validation of MODIS DT AODs against collocated AERONET (Levy  
376 et al., 2013). We show the percentage of AHI AODs that fall within the EE bounds.

377

378 Figure 2 shows the results of this validation for the over land retrieval, with Fig. 2a  
379 showing the scatterplot of the accumulation of all collocations for the duration of the time  
380 period investigated, and also specific panels showing the same, but for individual  
381 AERONET sites. The specific stations were chosen to represent three different

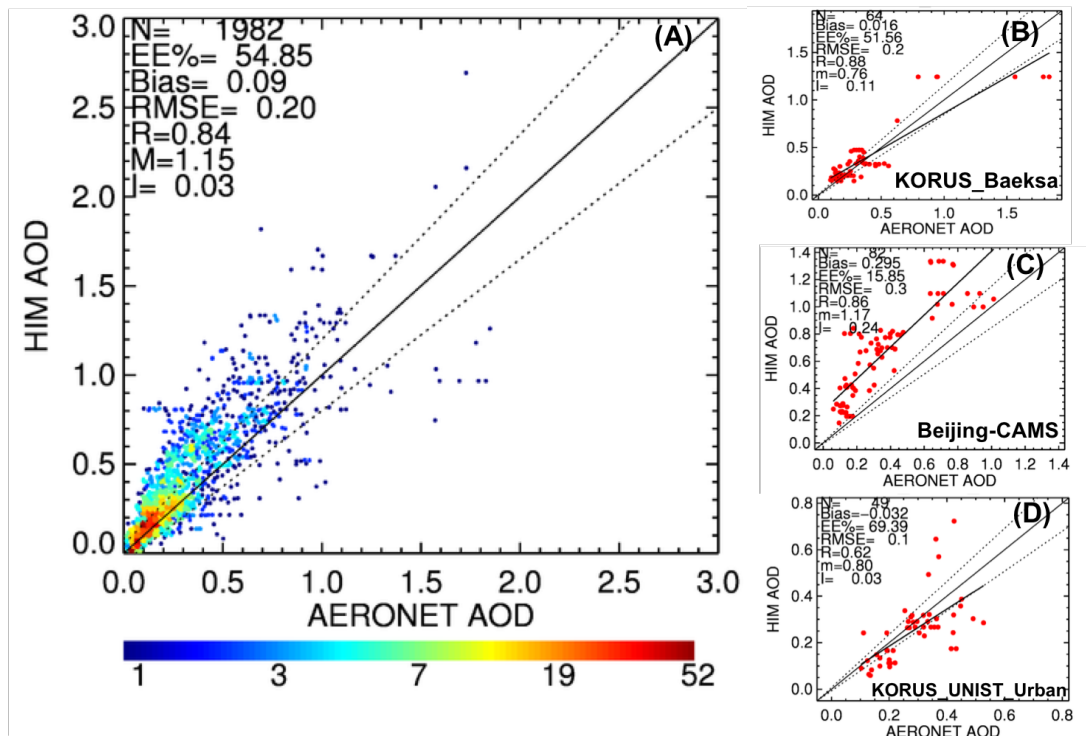


382 validation situations: when DT is biased high, biased low and unbiased against  
383 AERONET. Figure 3 shows the validation statistics calculated for each AERONET  
384 location within the AHI domain. Altogether there were 1982 collocations during the  
385 period of the study, with a dynamic range spanning AERONET-measured AOD from less  
386 than 0.05 to nearly 2. The AHI AODs match AERONET observations with a correlation  
387 coefficient of 0.84, a mean bias of 0.09 and RMSE of 0.20. Approximately 55% of the  
388 retrievals fall within the EE that was based on MODIS validation. Figure 3 shows that  
389 the distribution of validation statistics varies from stations to station, but that correlations  
390 tend to be overall high across mainland Asia, while biases, RMSE and percent within  
391 MODIS DT Expected Error vary more widely, even within tightly packed local networks.  
392

393 As a comparison, Figure 4 shows a similar set of plots, but for MODIS DT retrievals  
394 against AERONET. These collocations were made at the same stations as in Fig. 2, and  
395 over the same time period. Both Terra and Aqua are included. First, we see about half as  
396 many points as were seen in the AHI collocations because Terra and Aqua MODIS each  
397 pass over the area only once per day during daylight hours, while AHI is scanning these  
398 sites up to 9 times per day. Second, we notice that MODIS AODs match collocated  
399 AERONET AODs about the same as AHI AODs with  $R = 0.91$ , bias = 0.10, RMSE =  
400 0.19, and with 55% within EE. Only the correlation between MODIS and AERONET is  
401 substantially better than between AHI and AERONET.  
402

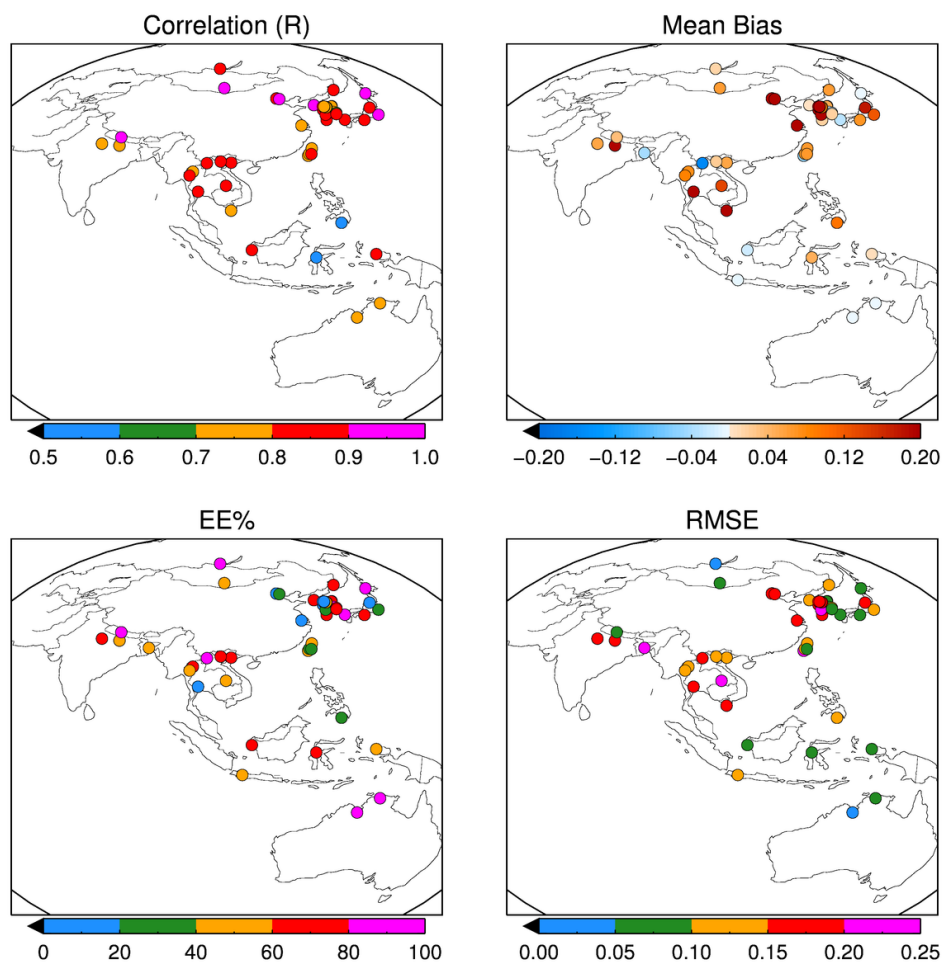
403 We see from this limited validation that the AHI-retrieved AOD is sufficiently accurate  
404 to represent the aerosol in this region, during this time period, approaching the same  
405 validation statistics as the durable MODIS product. We will next compare the full over  
406 lap of AHI-retrieved AOD with MODIS retrievals, regardless of AERONET.  
407

408  
409  
410



411  
 412  
 413  
 414  
 415  
 416  
 417  
 418  
 419  
 420  
 421  
 422  
 423

Figure 2. Density scatterplots of retrieved AOD at 550 nm derived from AHF radiances using the new DT AHF algorithm versus AOD at 550 nm spectrally interpolated from measured AODs from AERONET instruments collocated in time and space. Left panel A. All accumulated collocations in the AHF full disk domain over the 2 months study period May-June 2016. Right panels B, C and D, same for individual stations KORUS-Baeksa and KORUS-UNIST\_Ulsan in Korea and Beijing-CAMS in China. Shown in each panel are the number of collocations (N), percent within expected error as determined from MODIS DT analysis (EE%), mean bias (Bias), Root Mean Square Error (RMSE), correlation coefficient (R), slope (m) and intercept (l) of a linear regression equation through the points.

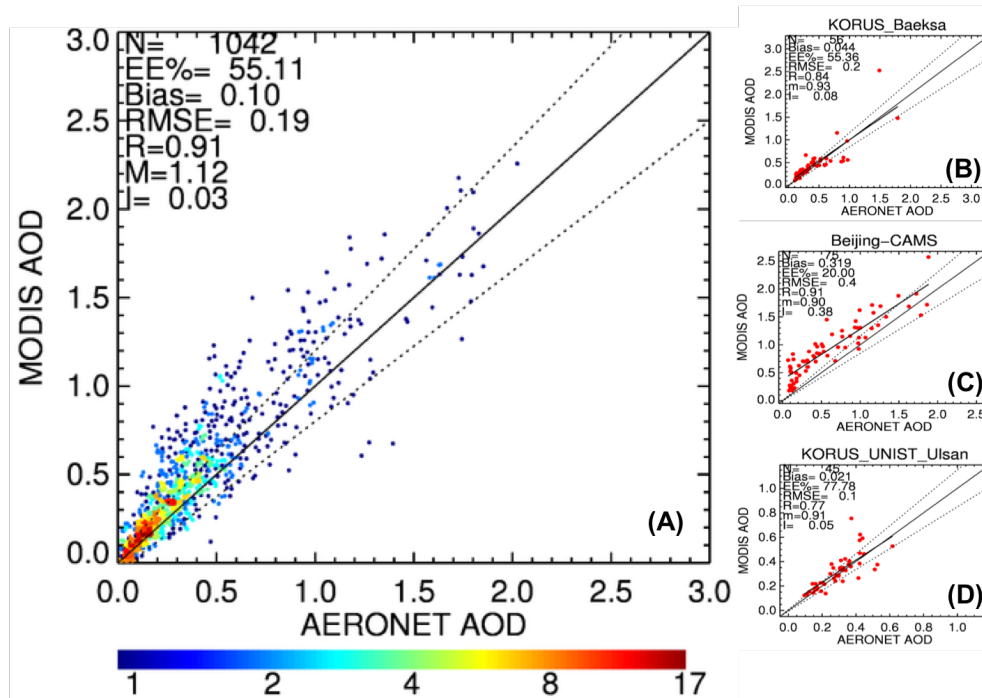


424

425

426 Figure 3. Spatial distribution of the collocation statistics between retrieved AOD at 550  
427 nm derived from AHI radiances using the new DT AHI algorithm versus AOD at 550 nm  
428 spectrally interpolated from measured AODs from AERONET instruments collocated in  
429 time and space. Shown are upper left: correlation (R); upper right: mean bias; lower left:  
430 Percentage within expected error (EE%); lower right: RMSE. Each point represents an  
431 AERONET station location.

432



433

434 Figure 4. Same as Figure 2 except now density scatterplots of retrieved AOD at 550 nm  
 435 derived from Terra and Aqua MODIS using the operational DT Collection 6.1 algorithm.  
 436 This data represents same stations and time period as shown in Fig2.

437

### 438 3.2 AHI versus MODIS DT

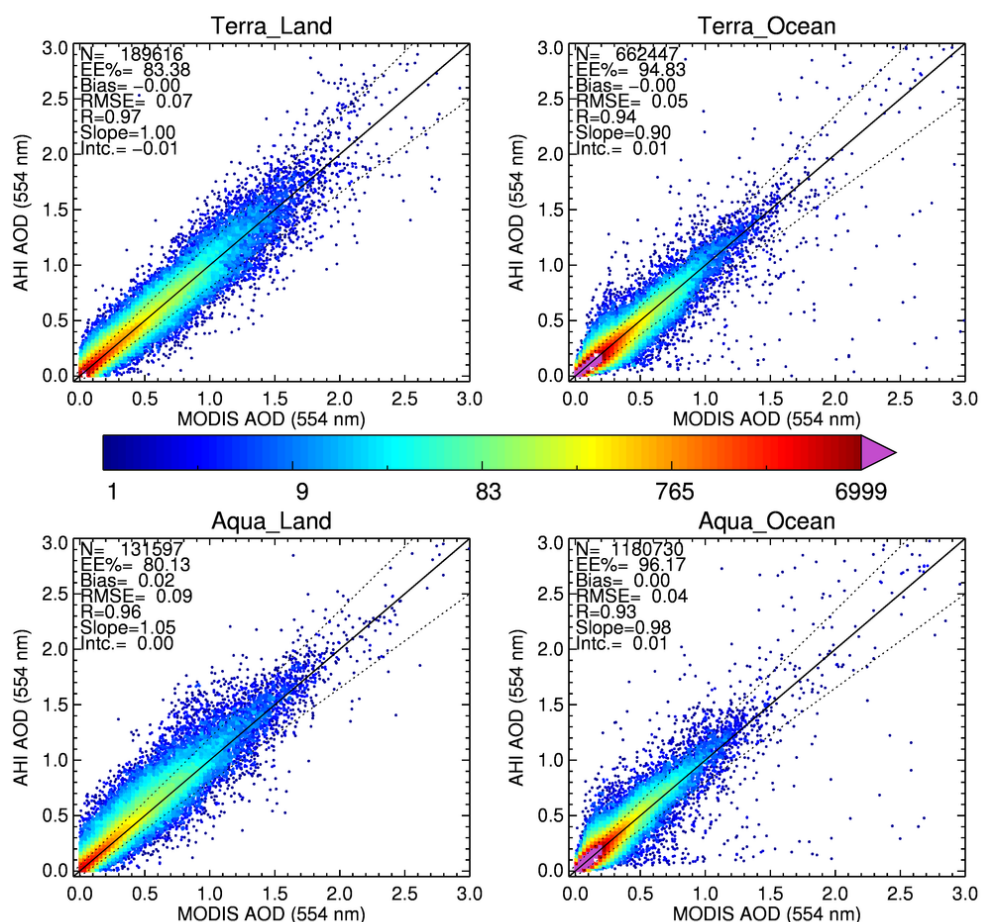
439

440 To collocate AHI and MODIS AOD, the Level 2 MODIS and AHI AOD data were  
 441 mapped to a common 0.25° latitude by 0.25° longitude grid for each AHI full disk scan.  
 442 To fill the grid, we include all MODIS retrievals within ±30 minutes of the AHI scan. All  
 443 the AOD retrievals falling within the above spatial and temporal windows were averaged  
 444 and statistics are retained for further analysis. It takes MODIS approximately 35-45  
 445 minutes to cut a poleward-to-poleward swath across an AHI image, and about 6-7 swaths  
 446 to transverse east-west across the disk. Thus, in the common grid, at any particular time,  
 447 while most of the grid has the possibility to include an AHI retrieval when cloud and glint  
 448 free, only a relatively small portion of the grid will be filled with MODIS retrievals to  
 449 create the possibility of a collocation.



450

451 Figure 5 presents the scatter plots from matching the products of the Terra/Aqua and AHI  
452 sensors on the common grid in each subset. Terra and Aqua collocations are kept  
453 separate, as are over land and over ocean retrievals. The DT AHI-retrieved AOD and the  
454 DT MODIS-retrieved AOD exhibit excellent correlation and similarity, as is expected  
455 from applying nearly the same retrieval algorithm to the radiance measurements of both  
456 sensors. Over ocean there are over 600,000 match-ups for Terra and over 1 million for  
457 Aqua. The geosynchronous AHI retrievals match the polar-orbiting MODIS retrievals  
458 with essentially zero bias and RMSE of 0.05 or less. Correlation between the two data  
459 sets is 0.93 or greater. Over land, there are over 100,000 match-ups for each satellite  
460 with no bias for Terra and 0.02 for Aqua, and RMSE of 0.09 or less. Correlations exceed  
461 0.95 over dynamic ranges from 0.0 to approximately 2.0. The plots in Figure 5 show  
462 how well the new AHI-retrieved AOD matches its MODIS counterpart when both AHI  
463 and MODIS offer retrievals for a particular time and location. These plots do not address  
464 situations in which a retrieval occurs for one satellite, but not the other, and therefore do  
465 not address typical retrieval issues such as cloud masking and choosing appropriate  
466 situations for the DT algorithm to make a retrieval. There can be also differences in  
467 AODs from two sensors due to difference in their viewing geometries. This is something  
468 beyond the scope of this paper and will be addressed in subsequent research.  
469



470

471 Figure 5. Density scatterplots of retrieved AOD at 554 nm derived from AHI radiances  
 472 using the new DT AHI algorithm versus retrieved AOD at 554 nm from the operational  
 473 MODIS Collection 6.1 algorithm, collocated in time and space. Top row are Terra  
 474 MODIS. Bottom row are Aqua MODIS. Left panels are results from the over land  
 475 retrieval. Right panels are results from the over ocean retrieval. The same collocation  
 476 statistics are displayed as in Figure 2.

477

478 Figure 6 shows the two-month mean AOD over the AHI disk from AHI and Aqua  
 479 MODIS, calculated from the data mapped to the common grid during our study period.



480 The mean AODs plotted here are collocated, and represent the AHI-derived AOD at  
481 approximately the same time as the MODIS overpass.

482

483 We see that the DT algorithm applied to both sensors results in very similar distributions  
484 of mean AOD across the AHI full disk image (Figure 6). This is despite the different  
485 sensor characteristics and very different viewing geometries. There is elevated aerosol  
486 across south and southeast Asia, and a separate pocket of elevated aerosol in northeast  
487 China. Low AOD occurs across most of the tropical and southern oceans. Australia is  
488 very clean and both sensors show a bit of moderately elevated AODs over the Indonesian  
489 island of Java. The magnitude of mean AOD in these images ranges from near 0.0 to  
490 almost 1.0.

491

492 The bottom panels of Figure 6 show the absolute differences in AOD when subtracting  
493 the top row MODIS panel from the top row AHI panel, and a similar difference map  
494 showing the differences between the top panel AHI values and a similar MODIS plot, but  
495 from the Terra satellite. The difference maps are AHI minus MODIS so that positive  
496 values, in red, indicate that AHI is higher than MODIS, while the negative values, in  
497 blue, indicate that AHI is lower than MODIS. The range of differences span +0.10 to  
498 about -0.08.

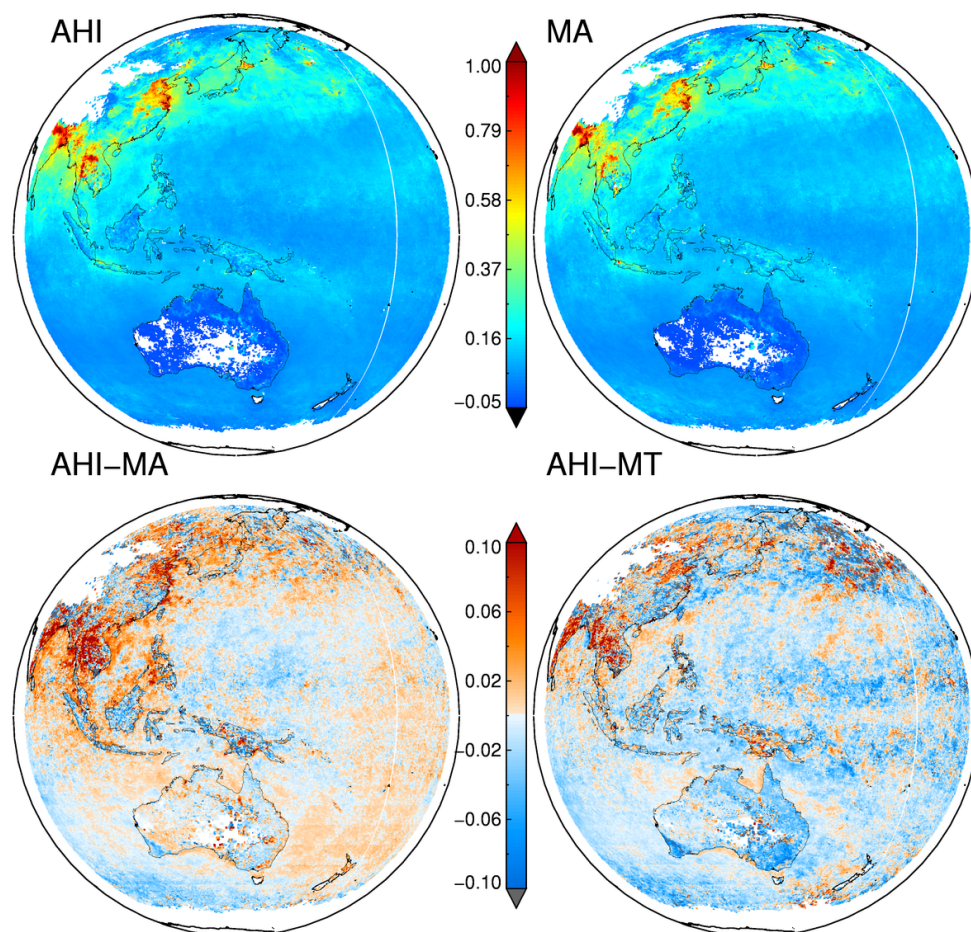
499

500 These plots indicate that over the elevated AOD regions, AHI retrievals are higher than  
501 MODIS retrievals by as much as 0.10. This higher AHI AOD is more prevalent and  
502 widespread with MODIS Aqua than with MODIS Terra. AHI tends to be about 0.02 to  
503 0.03 higher than MODIS Aqua over much of the ocean regions surrounding the Asian  
504 and maritime continents, while AHI tends to be closer to MODIS Terra in these regions  
505 and sometimes even negative. Over Australia, AHI is less than MODIS Terra by as  
506 much as -0.08. Because AOD values over Australia are very low to begin with, this  
507 negative with respect to MODIS Terra indicates that AHI retrievals over Australia are  
508 often absolutely negative more consistently than the MODIS retrievals and suggest that  
509 some adjustment to the surface parameterization in the AHI DT retrieval will be required.

510



511 The inconsistencies between the two difference maps, one showing AHI with respect to  
512 MODIS Aqua and the other with respect to MODIS Terra highlight the difficulty in  
513 producing consistent representations of the AOD field, even when applying the same  
514 algorithm to different sensors that should be exact duplicates of each other as in the case  
515 of MODIS Terra and MODIS Aqua (Levy et al., 2018). Given this inconsistency  
516 between the two MODIS instruments, the differences between AHI results and both  
517 MODIS instruments fall within expected and manageable ranges. The DT algorithm as  
518 applied to AHI is producing a representation of the spatial distribution of AOD with the  
519 same level of fidelity as the original DT MODIS algorithm. This is the first attempt of  
520 applying the DT algorithm to AHI, and we expect that future refinements to algorithm  
521 assumptions that account for specific instrument characteristics and calibration will bring  
522 AHI AOD results even closer to MODIS and AERONET values of AOD.  
523  
524



525

526

527 Figure 6. Top row: Mean AOD at 550 nm over the 2-month study period of May-June  
528 2016. Upper left: mean AOD derived from retrievals using the new DT AH1 algorithm  
529 applied to AH1. Upper right: mean AOD derived from the standard Aqua MODIS DT  
530 product. Bottom row: Difference maps of mean AOD at 550. Bottom left: Difference  
531 between the two maps in the top row. Bottom right: Similar difference map but between  
532 AOD from AH1 and AOD from Terra MODIS (MT), instead of Aqua MODIS (MA).

533

534

535

536



537 **4.0 Representation of AOD diurnal cycle using DT algorithm**

538

539 **4.1 Comparing AHI-derived diurnal signatures with AERONET**

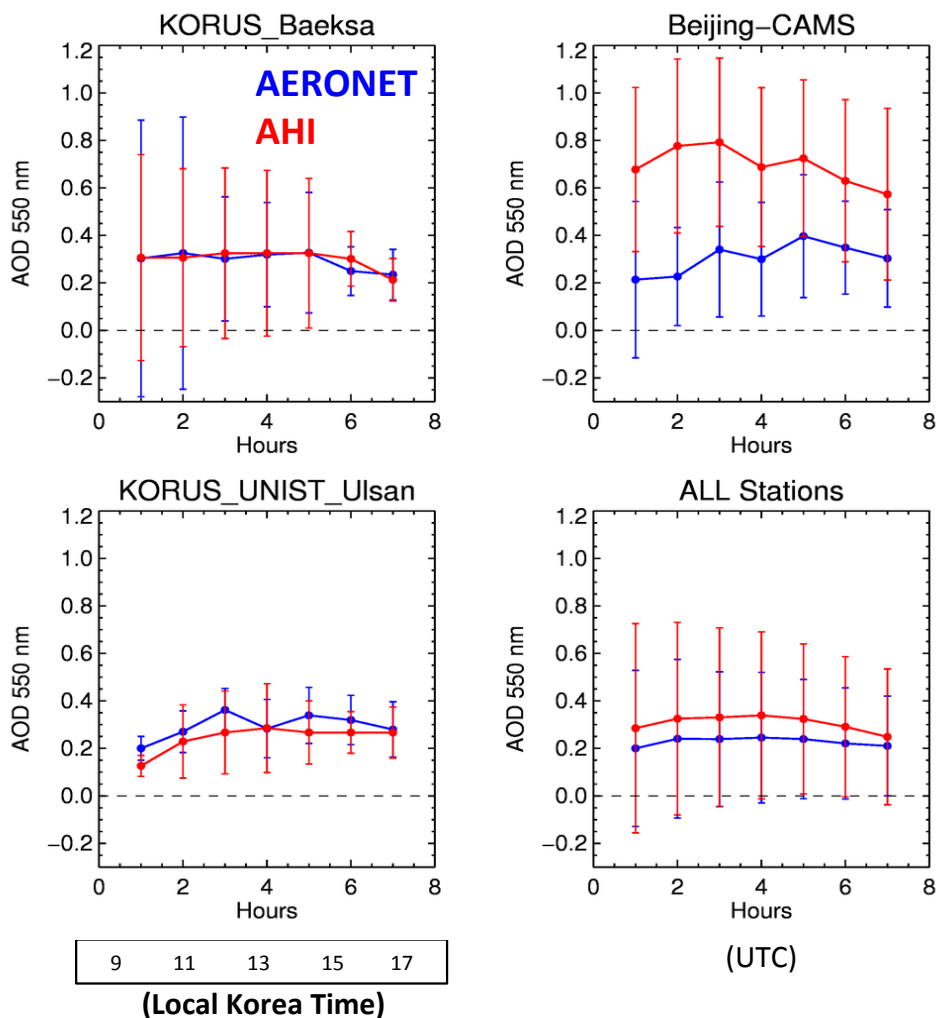
540

541 In the previous section we show how well the new DT AHI algorithm matches the AOD  
542 measurements from AERONET and the retrievals from MODIS. However, the point of  
543 applying an aerosol retrieval algorithm to a geosynchronous satellite sensor such as AHI  
544 is not to match the individual station data of AERONET nor the once-per-day retrievals  
545 from MODIS. The point of porting the DT aerosol algorithm to AHI is to represent the  
546 diurnal cycle of AOD over the broad regional area covered by the AHI full disk. In this  
547 section we explore the diurnal cycle of AOD derived from AHI and evaluate how much  
548 of the aerosol system MODIS has been missing because of its limited temporal sampling.  
549

550 The diurnal cycle of AHI-derived AOD is compared with collocated diurnal patterns of  
551 AOD exhibited by AERONET stations within the AHI full disk image. The diurnal cycle  
552 at each AERONET station was calculated by finding the mean AERONET AOD at seven  
553 specific times of the day corresponding to the time of an AHI scan. These times are  
554 01:00, 02:00, 03:00, 04:00, 05:00, 06:00 and 07:00 UTC, corresponding to the hours of  
555 10:00 to 16:00 in local Korean time. All AERONET AOD measurements  $\pm 30$  minutes of  
556 the nominal time were included in the average to represent the mean AOD at the nominal  
557 time. In parallel, the mean AOD at these specific times were calculated from all AHI-  
558 derived AOD located within a  $0.25 \times 0.25$  degree box around the AERONET station for all  
559 AHI scans taken at the nominal time. Thus, we created two representations of the diurnal  
560 cycle of AOD at each AERONET station, one from AERONET data and one from AHI-  
561 derived data, all from the collocation data set. This means that both AERONET and AHI  
562 must report at the same specific time for the instruments' AOD to be included in the  
563 calculated hourly average. This is the purest means to compare the actual retrieval, but  
564 will not reveal differences in sampling factors such as cloud masking because AHI will  
565 benefit from AERONET's cloud identification.

566

567



568  
 569 Figure 7. Median AOD at 550 nm in each of 7 time-of-day bins corresponding to 10:00 to  
 570 16:00 Korean standard time. Shown are three individual AERONET stations and also  
 571 (lower right) the results of binning all of the AERONET stations across the full disk  
 572 image as shown in Figure 3. Red indicates AOD derived from AHI using the new DT  
 573 algorithm. Blue indicates AOD measured by AERONET. The statistics were calculated  
 574 from the collocation data base such that each bin contains the same number of  
 575 observations from AHI and AERONET taken at the same time, although the number of  
 576 observations in each diurnal bin will differ. Vertical error bars represent one standard  
 577 deviation among different days for the same hour.



578 Figure 7 shows the calculated median AOD diurnal cycles from AERONET and AHI-  
579 retrievals for three individual stations in Korea and China, and also the median of all  
580 stations located in the AHI full disk image and reporting during our period of study. Error  
581 bars represent the standard deviation of the sample in each hourly bin. At the three  
582 stations shown individually in Figure 7, we see that the same biases seen in Figure 2 also  
583 appear here, particularly with Beijing CAMS showing a strong positive bias. There is  
584 wide scatter in the AOD for each hourly bin, as portrayed by the relatively large error  
585 bars. The diurnal pattern of AOD, as measured by AERONET at KORUS Baeksa shows  
586 a sudden decrease after 0500 UTC (14:00 Korea Standard Time), dropping from a steady  
587 0.3 to 0.2 in two hours. The AHI AOD retrievals match this pattern almost exactly. The  
588 other Korean station, KORUS\_UNIIST\_Ulsan, shows an opposite daily pattern, with  
589 AOD increasing from a morning low of 0.2 at 0100 UTC (10:00 Korean Standard Time)  
590 to 0.3-0.4 at midday and then a drop off towards evening. The AHI AOD at this station is  
591 biased low throughout most of the day, but does reflect the same diurnal signature of  
592 increasing AOD over the morning. At the third station, Beijing CAMS, the AHI AOD  
593 diurnal pattern does not match AERONET as well, but there is a strong positive bias  
594 there with very large scatter in each hour. With error bars spanning 0.5 AOD, it is  
595 difficult to discern diurnal changes with amplitudes of 0.2 AOD or less in either  
596 AERONET or AHI.

597

598 The diurnal analysis shown in Figure 7 suffers from relatively small data samples. The  
599 number of collocations for KORUS\_Baeksa, KORUS\_UNIST\_Ulsan and  
600 Beijing\_CAMS are 56, 45 and 75, respectively, distributed over 7 hourly bins. If clouds  
601 were not a factor, each hourly bin median might be constructed from only 6 to 11  
602 samples. However, clouds are indeed a factor, with their own diurnal patterns. The  
603 actual number of AHI-AERONET collocations at any particular hour might be as few as  
604 3, and morning and afternoon bins reported in Figure 7 might be constructed from  
605 entirely different days. Therefore, the diurnal patterns in Figure 7 may be artificial  
606 composites and not representative of the actual changes in AOD over the course of a  
607 single day. However, the point of this comparison is not to speculate on the cause of the



608 diurnal signatures, but to establish that the AHI-derived AOD has the ability to describe  
609 the same mean diurnal pattern in the aerosol as AERONET for individual locations.

610

611 The ensemble statistics of the diurnal signature for all AERONET stations and collocated  
612 AHI retrievals in the AHI full disk image show the high bias of the AHI retrievals, as per  
613 Figure 2, but also that the ensemble mean diurnal signature of AHI AOD is mostly flat, as  
614 is the diurnal signature from AERONET. Both AHI and AERONET AOD exhibit a  
615 slight increase in AOD from morning to midday. Then, AHI decreases towards the end of  
616 the day, while AERONET stays flat. The scatter in each hourly bin is large, as shown by  
617 error bars that span 0.6 in AOD, and thus diurnal patterns with amplitudes of 0.1,  
618 exhibited by both AHI and AERONET fall well below a significant signal to noise  
619 threshold. Still the basic agreement of AHI to AERONET in the overall ensemble diurnal  
620 statistics is encouraging.

621

#### 622 **4.2 Full disk AHI-derived AOD diurnal cycle**

623

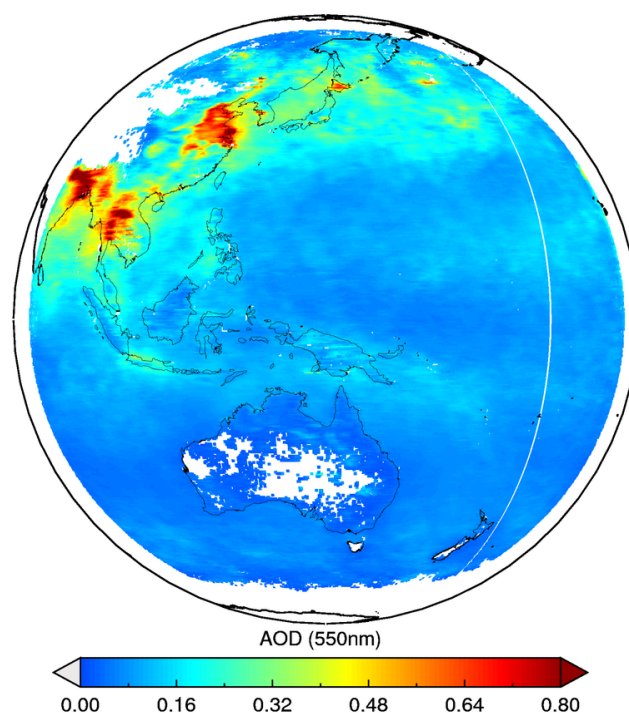
624 Previously, Figure 6 showed the mean full disk AHI AOD calculated for the approximate  
625 times of the MODIS overpasses. Now we calculate the overall mean AHI-derived AOD  
626 calculated over the entire day time diurnal cycle and not just at MODIS overpass time,  
627 for the duration of our study period at each of the  $0.25^\circ$  latitude by  $0.25^\circ$  longitude grid  
628 squares. Figure 8 shows this overall period mean map, with all diurnal information lost.  
629 The period mean map at MODIS overpass time (Figure 6) looks qualitatively very similar  
630 to the overall period mean map (Figure 8), suggesting that MODIS sampling provides a  
631 good representation of the overall AOD distribution.

632

633



634  
635  
636  
637  
638  
639  
640  
641  
642  
643  
644  
645  
646  
647  
648  
649  
650  
651



652 Figure 8. Daily mean AOD at 550 nm calculated over all daylight full disk images of  
653 AHI during May-June 2016. No requirements of collocation with MODIS or AERONET  
654 were imposed.

655  
656 Then we calculate the mean AOD for each AHI full disk scan corresponding to a  
657 particular UTC hour, in each grid over the period of our study. Figure 9 shows the plots  
658 of the absolute difference (mean hourly AOD minus mean daily AOD) at each of these  
659 diurnal hours.

660  
661 Figure 9 captures the diurnal signature of the aerosol over a broad region of Earth. Red  
662 colors indicate that at a particular hour of the day, the AOD is higher than the daily mean.  
663 Blue colors indicate that the hourly AOD is lower than the daily mean. The large gray  
664 circle that traverses the image from hour to hour is the glint mask preventing the over



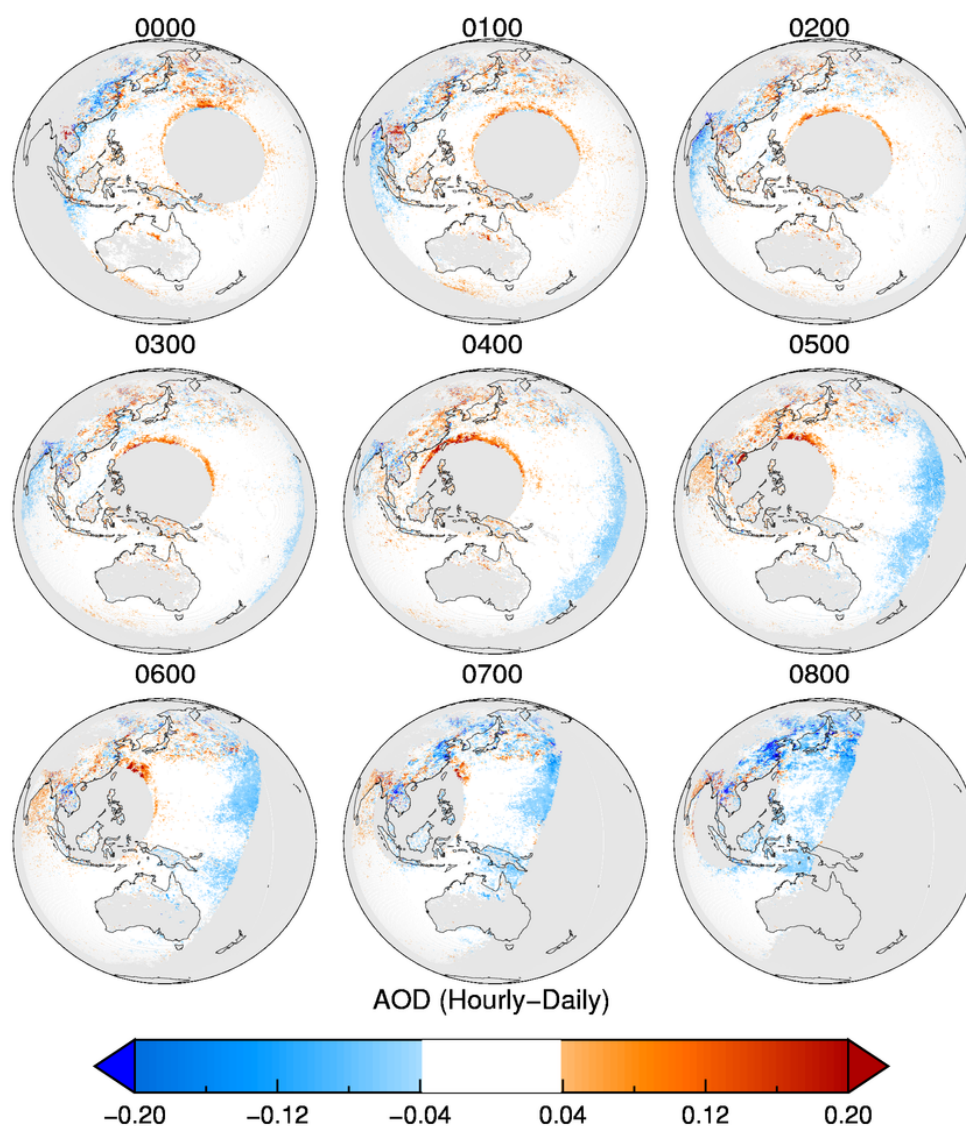
665 ocean algorithm from retrieving an AOD value. The glint mask is set for glint angles <  
666 40°, which unfortunately eliminates large portions of a geosynchronous image from being  
667 suitable for a DT aerosol retrieval. The glint mask proceeds across the image hour by  
668 hour so that the glint mask becomes indiscernible in the daily mean. That is why there is  
669 no apparent glint mask in the overall daily average of Figure 8, nor in Figure 6,  
670 constructed from AHI AOD collocated with MODIS. Continents and islands within the  
671 glint mask will call on the over land DT algorithm that does not mask for glint, and  
672 therefore, will return an AOD value.

673  
674 The most striking feature in Figure 9 is the blue shading at the edges of the over ocean  
675 retrieval domains that begin the day to the west in the Indian Ocean and then switch to  
676 the east in the Pacific in the afternoon. This band of “lower than daily average” AOD is  
677 associated with solar zenith angle, not view angle, as it hugs the day/night terminator in  
678 the images, even when that terminator crosses the center of the full disk image. By 0700  
679 and 0800 UTC, the terminator artifact encompasses a broad geographical swath of ocean,  
680 which would introduce an incorrect interpretation of local diurnal AOD signal with  
681 amplitudes of 0.15, when daily mean values are only 0.10. Such strong diurnal swings in  
682 AOD over the remote ocean on global scales are unrealistic.

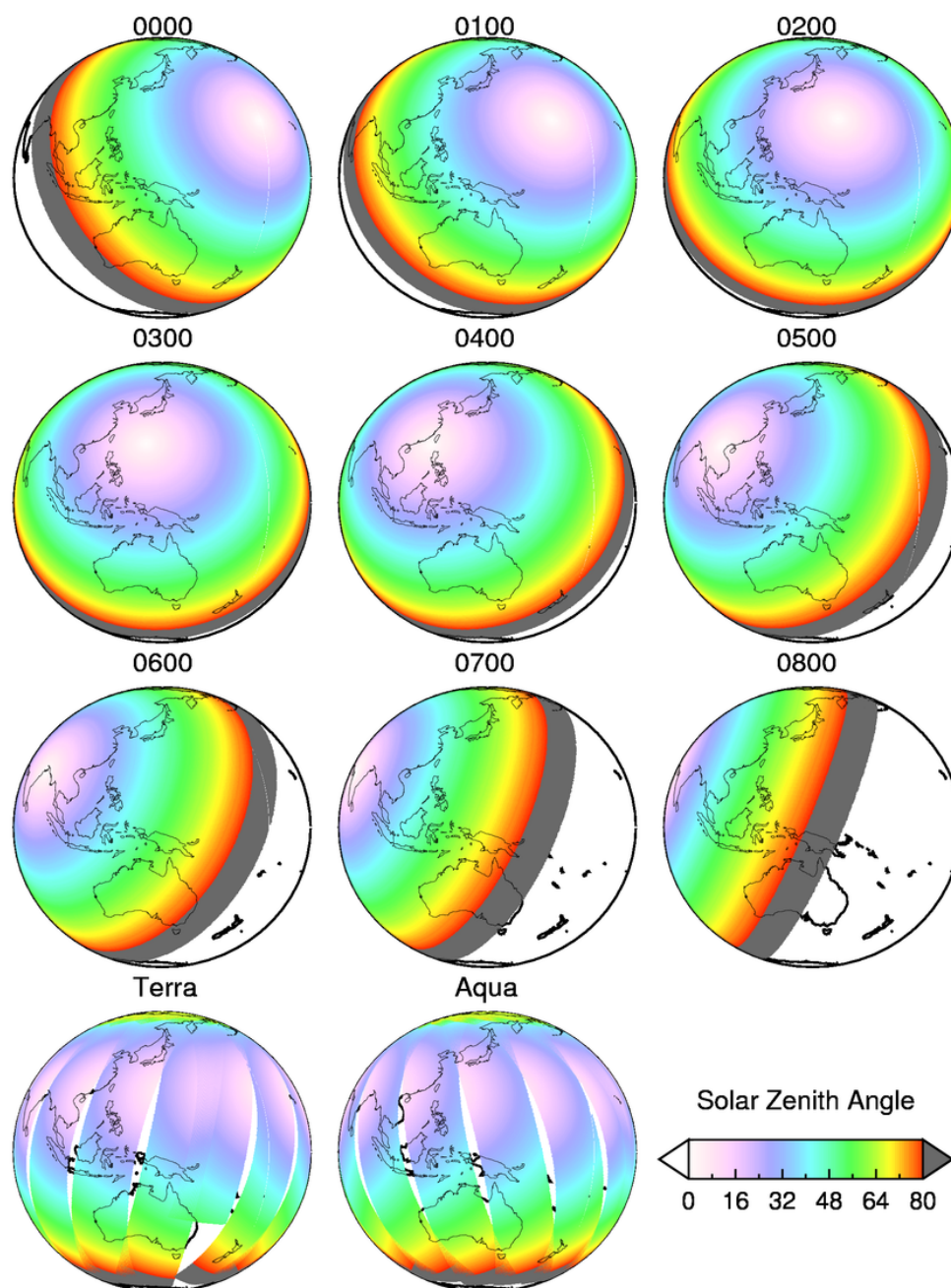
683  
684 The problem may be introduced by the radiative transfer code used to create the Look Up  
685 Tables for the over ocean retrieval (Ahmad and Fraser, 1982) that does not fully account  
686 for Earth’s curvature. Although this code has served the DT retrieval well through the  
687 MODIS and VIIRS eras, those polar orbiting satellites only encounter extreme solar  
688 zenith angles at the beginning and end of their orbits near the poles, where DT aerosol  
689 retrievals are rare due to other factors such as extreme cloudiness or snow/ice. The  
690 inability to properly model Earth’s sphericity is likely to be of greater concern for  
691 geosynchronous satellites that encounter extreme solar zenith angles across all latitudes  
692 and in prime retrieval areas. See Figure 10. Currently the AHI DT algorithm retrieves all  
693 geometries with solar zenith angle < 80 degrees. Figures 9 and 10 suggest that the  
694 terminator artifact could be mitigated by applying a more stringent threshold of 70



695 degrees. However, development and application of a spherical radiative transfer code is  
696 the more satisfying long-term solution.  
697



698  
699 Figure 9. Difference in hourly mean AOD at 550 nm as derived from the new DT AHI  
700 algorithm from the daily mean AOD, as plotted in Figure 8. Red indicates the specific  
701 hour has higher AOD than the daily mean, and blue indicates the opposite.  
702



703

704

705 Figure 10. Mean solar zenith angle associated with each of the diurnal hours from the

706 AHI geometry and also for MODIS on Terra and Aqua for May 29, 2016.



707 There also appears to be another AOD retrieval artifact over the ocean associated with the  
708 glint angle. Here AODs seem artificially high. Incorrect estimation of wind speed from  
709 ancillary data or modeling of the rough ocean surface will introduce near-glint mask  
710 inaccuracies in the AOD retrieval. With MODIS, such areas were relatively small and  
711 the overall effect on global or regional AOD minimal. In the geosynchronous view,  
712 because the glint mask is such a dominant feature, the near-glint artifacts appear much  
713 more pronounced.

714

715 The good news seen in Figure 9 is that the retrieval over land does not appear to have  
716 encountered any systematic artifacts. Blue and red shading is distributed spottedly across  
717 the Asian, Indonesian and Australian land masses. Without validation we cannot say for  
718 sure, but typically local factors determine aerosol diurnal trends, and thus, the spotty  
719 blue/red shading could indicate that the retrieved AOD is representing the consequences  
720 of these local diurnal forcing mechanisms. We have already seen in Figure 7 that the  
721 AHI retrievals resolved the differing local diurnal patterns at three over land AERONET  
722 stations within relative close proximity. In terms of the over land retrieval, Figure 9  
723 demonstrates that the DT algorithm applied to AHI will identify land regions where the  
724 diurnal signal is more spatially cohesive. For example the east coast of India and  
725 Bangladesh experience an increase in AOD in the late afternoon, while the overall trend  
726 in northeast China is to decrease AOD in the afternoon, although there are local  
727 contradictions to these regional patterns.

728

#### 729 **4.3 AHI-derived AOD diurnal cycle over 5-degree squares**

730

731 The factors that drive a diurnal AOD signature tend to be local in character. These  
732 include sources and sinks linked to time-of-day (rush hour traffic, agricultural burning,  
733 afternoon convection/precipitation) or diurnally influenced mesoscale circulations and  
734 transport (sea breeze or mountain slope regimes). Thus, individual stations as shown in  
735 Figure 7 exhibit stronger diurnal signatures than does an ensemble average consisting of  
736 stations distributed across the region (bottom right panel of Figure 7). The full disk plots  
737 of Figure 9 suggest that there are regions of moderate extent that do experience a



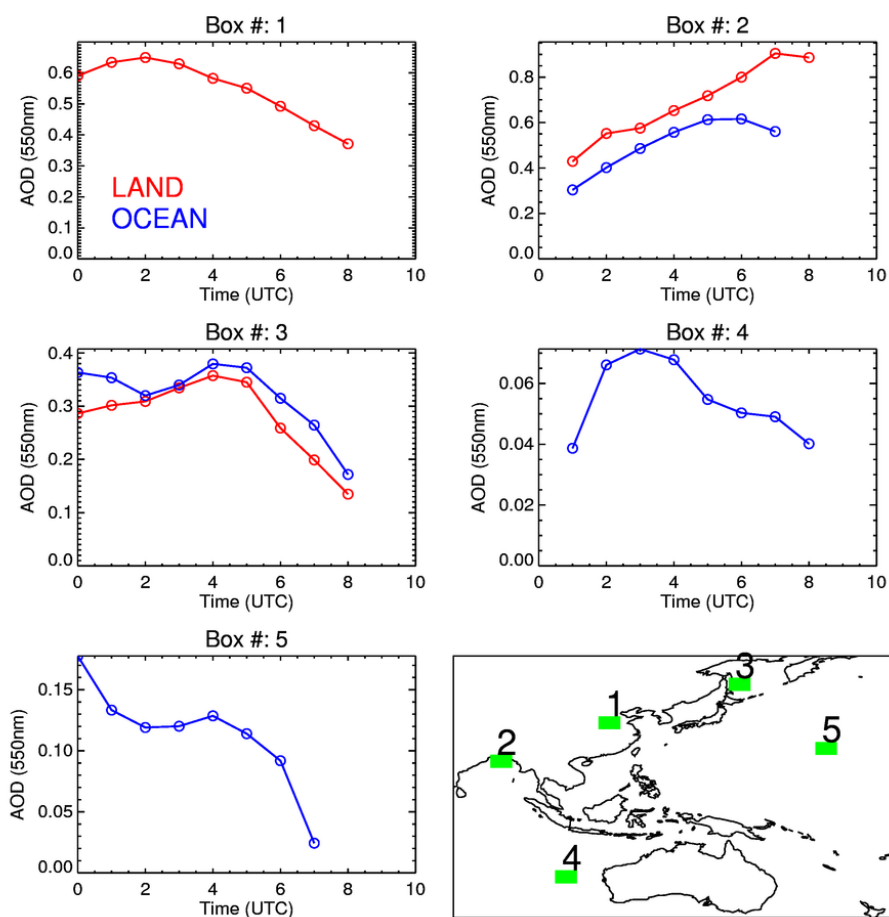
738 cohesive diurnal AOD pattern. To further investigate the ability of the DT AHI to provide  
739 insight into diurnal patterns of AOD during daylight hours we calculate the average AOD  
740 in specific 5° latitude by 5° longitude boxes as a function of the hour of the day.

741

742 Figure 11 shows the diurnal AOD signatures of five of these 5° by 5° boxes. As suggested  
743 by Figure 9, the AOD over northeastern China (Fig. 11, Box# 1) exhibits its highest AOD  
744 during morning hours, 00 UTC to 03 UTC, corresponding to local times of 0800 to 1100,  
745 then experiences a slow decrease during the remainder of the day until sunset. Average  
746 mean AOD at 550 nm in this area ranges from morning values of 0.65 to late afternoon  
747 values of less than 0.40. Over Bangladesh (Fig. 11, Box #2) the glint mask does not  
748 interrupt ocean retrievals until the last diurnal hour of the day. Ocean and land retrievals  
749 exhibit very similar diurnal signatures in this area, slowly rising from morning lows of  
750 0.3-0.4 to late afternoon highs of 0.8-0.9, at least over land. Another area containing both  
751 land and ocean retrievals is over northern Japan and adjacent Pacific Ocean (Fig. 11, Box  
752 #3). This area is far enough north to not be hampered by the glint mask at this time of  
753 year. The over ocean and over land diurnal patterns are similar with morning to midday  
754 values of 0.30-0.35 gradually decreasing through the afternoon to lows of 0.15 by sunset.  
755 This is a significant diurnal range of AOD over ocean.

756

757



758

759

760 Figure 11. Spatially averaged mean AOD at 550 nm from the derived DT AHI product  
 761 for selected 5° by 5° latitude-longitude squares (boxes) in each hourly bin for the two-  
 762 month study period, producing AOD diurnal signatures for these selected areas. Red lines  
 763 depict over land retrievals. Blue lines depict over ocean retrievals. X-axes are in UTC  
 764 hours, for the reference, the local time in Beijing is +8 hours from UTC. Y-axes scale  
 765 vary from plot to plot. The green squares on global map indicates location of the specific  
 766 box.

767

768 Two areas over open ocean are shown in Figure 11, one in the Indian ocean west of  
 769 Australia (Fig. 11 Box #4) and the other in the Pacific (Fig. 11, Box #5). Note that the



770 scales on the y-axes of these two plots are different. At the Indian ocean area there  
771 appears to be a diurnal signal, but the amplitude of that signal is only about 0.02, well  
772 within the noise levels of both the retrieval itself and of the sampling and statistics of  
773 calculating the diurnal pattern. Essentially there is no significant diurnal signal at this  
774 location and the mean AOD is about  $0.05 \pm 0.01$ . In contrast the Pacific example exhibits  
775 a strong diurnal pattern, ranging almost an order of magnitude from 0.18 ( $\sim 0.2$ ) to 0.02.  
776 It is in this area that the two ocean artifacts become apparent. During the early morning  
777 hours this area resides just north of the sun glint mask where insufficient modeling of the  
778 rough ocean surface creates an artifact in the retrieval, introducing a high bias. During  
779 late afternoon hours, the solar zenith angle increases to beyond  $70^\circ$  and the low bias  
780 artifact from the terminator affects the retrieval. It is only midday day when this Pacific  
781 region escapes either artifact and then we see little diurnal signature and a mean AOD of  
782  $0.11 \pm 0.015$ . Thus, the apparently strong diurnal signal here is in reality just the  
783 combination of two different artifacts in the retrieval.

784

785 The examples in Figure 11 illustrate the variety of aerosol diurnal patterns over Asia with  
786 polluted regions like northeastern China and Bangladesh showing diurnal amplitudes of  
787  $0.25 - 0.50$  in AOD, but with oppositely signed slopes. The need to understand and  
788 explain these different patterns across an area as large as Asia opens new research  
789 questions as to what is the driving processes behind these AOD patterns, how will they  
790 affect assimilation into global and regional models, and what are the air quality and  
791 public health implications? While the processes creating diurnal aerosol patterns are  
792 primarily local, the consequences of spatially cohesive patterns will have non-local  
793 consequences, and aerosol products from geosynchronous observations, such as the AHI  
794 DT product, are key to identifying and quantifying these spatially cohesive situations.  
795 The patterns seen in Figure 11 may also suffer from the caveats imposed upon the  
796 individual station analysis of Figure 7, The diurnal patterns may be artificial constructs of  
797 observations made at different times on different days and not represent the true change  
798 of aerosol loading over the span of day light hours. However, because of the greater  
799 statistical sample offered by the larger spatial domain of the  $5^\circ \times 5^\circ$  box there is greater  
800 confidence in the patterns of Figure 11 than those of Figure 7.



801 The examples in Figure 11 also illustrate that artifacts still exist in the retrieval over the  
802 ocean, but that not all strong diurnal signatures over ocean are due to the artifacts, as  
803 shown in Fig. 11d where the ocean pattern mimics the artifact-free land pattern. Being  
804 aware of the possibility of artifacts and working towards mitigating those artifacts in the  
805 future will be essential to properly making use of any new geosynchronous product.

806

## 807 **5.0 Discussion and conclusions**

808

809 The traditional Dark Target (DT) aerosol retrieval algorithm was adapted for the  
810 Advanced Himawari Imager (AHI) and applied to AHI-measured spectral reflectances for  
811 the two-month period of May-June 2016. The adaptation makes use of the spectral  
812 similarity between AHI and its predecessor DT sensors (e.g. MODIS, VIIRS), but omits  
813 certain important pixel selection procedures that require spectral bands unavailable from  
814 AHI. The lack of these specific masks may permit additional cirrus and cloud  
815 contamination into the results of this two-month preliminary demonstration, although  
816 large-scale comparisons of collocated AHI and AERONET or AHI and MODIS retrievals  
817 do not reveal significant overall biases. However, AHI retrievals may be benefitting from  
818 AERONET or MODIS cloud masking in the collocations. Expanding the AHI retrieval  
819 into the winter months when snow/ice will be encountered will then certainly show  
820 contamination from such surfaces, as the current DT snow/ice mask requires the 1.24  $\mu\text{m}$   
821 channel that is missing from AHI. Before wintertime retrievals are made with AHI, a new  
822 cloud/ice mask for this sensor must be developed.

823

824 Collocations between AHI and AERONET demonstrate that AHI retrievals match  
825 AOD<sub>550 nm</sub> at AERONET stations as well as the MODIS DT aerosol product matches  
826 AERONET in terms of correlation, RMSE, overall bias and percentage within expected  
827 error. Additionally, because AHI can make aerosol retrievals multiple times per day,  
828 there were approximately twice as many AHI-AERONET collocations as there were  
829 from MODIS-AERONET. Geostationary aerosol retrievals will significantly increase the  
830 sampling of retrieved AOD from current polar-orbiting sensors. Not only did the DT AHI  
831 product match AERONET, statistically, in scatterplots, it also represented the diurnal



832 signal in AOD, as measured by AERONET at individual stations, and in the ensemble  
833 median statistics. The three stations shown are representative of varying retrieval biases  
834 and exhibit different diurnal signatures, even though they are in relatively close  
835 proximity. The AHI DT algorithm was able to distinguish these diurnal differences,  
836 although sample size was small and signal-to-noise impeded inference of the diurnal  
837 signature.

838

839 Collocated AHI and MODIS retrievals demonstrate excellent agreement when applying  
840 the DT algorithm to the two different sensors. Both AHI and MODIS produce similar  
841 representations of the 2-month mean AOD across the AHI full disk region. However,  
842 difference maps do show regional biases. Interestingly, AHI is overall biased low against  
843 MODIS-Terra, but biased high against MODIS-Aqua, and thus falling within the offsets  
844 already noted between the AODs of the two MODIS sensors (Levy et al., 2018). The one  
845 place that AHI differs in the same way from both MODIS-Terra and MODIS-Aqua is in  
846 its positive bias of 0.10 in the high aerosol loading regions of south, southeast and  
847 northeast Asia. The fact that these biases are only seen in high aerosol loading suggests a  
848 problem with the traditional DT aerosol models, not the surface parameterization. We  
849 note that the over land aerosol models have never been tested for the unique geometry  
850 that AHI has brought to the table.

851

852 When the algorithm is applied to the full disk image and hourly mean AOD plots are  
853 made, we notice immediately an artifact in the diurnal signature that affects only the over  
854 ocean retrieval. This artifact occurs at the day/night terminator and is associated with  
855 extreme solar zenith angles, not view angles. Extreme solar zenith angles are much more  
856 prevalent in geosynchronous images than in polar-orbiting ones, and thus our previous  
857 experience with polar-orbiting sensors did not prepare us for this artifact. The most likely  
858 explanation for the solar zenith artifact is the inability of the original radiative transfer  
859 code to model spherical Earth. Earth's curvature when the sun is on the horizon will  
860 introduce uncertainties into the radiative transfer calculation and result in inaccurate  
861 aerosol retrievals. Until modifications can be made to the radiative transfer code, the  
862 solution to mitigating this artifact will be to limit retrievals to lower solar zenith angles



863 over ocean ( $<70^\circ$ ). This is unfortunate because already the retrieval loses a goodly  
864 section of the equatorial ocean because of the  $40^\circ$  glint mask when solar zenith angles are  
865 small. Because we also saw retrieval artifacts along the edge of the glint mask, it is  
866 unlikely that the  $40^\circ$  threshold can be relaxed. For now, the DT AHI retrieval over ocean  
867 should be limited to a small range of solar zenith angles that will avoid both the glint and  
868 the artifact at the terminator, and this will limit the diurnal range of AHI-retrieved AOD  
869 over ocean.

870

871 In a preliminary analysis meant to show the scientific potential of the AHI DT product  
872 we found a balance between the local nature of diurnal signatures and the need of a  
873 substantial statistical sample by calculating the mean diurnal patterns of AOD in  $5^\circ$   
874 latitude by  $5^\circ$  longitude boxes. The result of this analysis revealed a variety of diurnal  
875 patterns across Asia, as well as illustrating diurnal patterns of ocean areas affected and  
876 not affected by glint and solar zenith angle artifacts. A more mature AHI DT product  
877 will enable further exploration of these diurnal patterns and the consequences these  
878 patterns hold for climate processes, assimilation systems and air quality.

879

880 To make progress towards a more mature algorithm beyond the preliminary version  
881 analyzed here, we will need to continue the analysis and investigate the following points:

882

- 883 • What is the reason for the biases between AHI and both AERONET and MODIS?
- 884 • Are these biases linked to solar zenith angle, view angle or scattering angle?
- 885 • Are these biases linked to surface parameterization? Specifically change in  
886 surface ratios with viewing geometry.
- 887 • Do we mitigate artifacts by employing a more realistic spherical radiative transfer  
888 code?
- 889 • How do we mask for snow/ice without the  $1.24\ \mu\text{m}$  wavelength?
- 890 • Can we characterize cloud and cirrus contamination in the retrievals, and then  
891 mitigate those effects?
- 892 • How does the retrieved AOD spectral dependence and size parameter from AHI  
893 compare to those from MODIS?



- 894       • Can we surpass results obtained from the polar orbiting sensors by incorporating  
895           additional specific geosynchronous capabilities into the DT retrieval?

896

897 The short two-month demonstration described and illustrated here is a preliminary  
898 assessment of the ability to bring the well-vetted DT aerosol retrieval to a  
899 geosynchronous satellite sensor. The results show that porting the algorithm is possible,  
900 that it can produce AOD that matches AERONET to the same degree as the MODIS  
901 product, and that it can distinguish local diurnal signatures at AERONET stations over  
902 land. The view from geosynchronous sensors will provide new insight into Earth's  
903 aerosol system, especially if that view is steeped in and compatible with the 20-year  
904 record of the DT polar-orbiting experience. This study puts us on the road to achieving  
905 this new perspective.

906

## 907 **6. Acknowledgement**

908

909 This work was supported by the NASA ROSES program NNH17ZDA001N: Making  
910 Earth System Data Records for Use in Research Environments and NASA's EOS  
911 program managed by Hal Maring. We thank Space Science and Engineering Center  
912 (SSEC), University of Wisconsin-Madison for providing Himawari-8 data. We thank  
913 MCST for their efforts to maintain and improve the radiometric quality of MODIS data,  
914 and LAADS/MODAPS for the continued processing of the MODIS products. The  
915 AERONET team (GSFC and site PIs) are thanked for the creation and continued  
916 stewardship of the sun photometer data record; which is available from  
917 <http://aeronet.gsfc.nasa.gov>.

918

919

## 920 **7. References**

921

922 Ahmad Z. and Fraser R.: An iterative radiative transfer code for ocean-atmosphere  
923 systems, *J. Atmos. Sci.*,32, 656-665, doi:10.1175/1520-0469(1982)039, 1982.



- 924 Boucher, O., et al.: Clouds and aerosols. In: Climate Change 2013: The Physical Science  
925 Basis. Contribution of Working Group I to the Fifth Assessment Report of the  
926 Intergovernmental Panel on Climate Change [Stocker, T. F., D. Qin, G.-K. Plattner,  
927 M. Tignor, S. K. Allen, J. Boschung, A. Nauels, Y. Xia, V. Bex, and P. M. Midgley  
928 (eds.)]. Cambridge University Press, Cambridge, United Kingdom and New York,  
929 NY, USA, 2013.
- 930 Diner, D. J., Beckert, J. C., Reilly, T. H., Bruegge, C. J., Conel, J. E., Kahn, R. A.,  
931 Martonchik, J. V., Ackerman, T. P., Davies, R., Gerstl, S. A. W., Gordon, H. R.,  
932 Muller, J.-P., Myneni, R. B., Sellers, P. J., Pinty, B., and Verstraete, M. M.: Multi-  
933 angle Imaging SpectroRadiometer (MISR) instrument description and experiment  
934 overview, *IEEE T. Geosci. Remote*, 36, 1072–1087, doi:10.1109/36.700992, 1998.
- 935 Diner, D. J., Abdou, W. A., Ackerman, T. P., Crean, K., Gordon, H. R., Kahn, R. A.,  
936 Martonchik, J. V., McMuldroy, S., Paradise, S. R., Pinty, B., Verstraete, M. M.,  
937 Wang, M., and West, R. A.: Multi-Angle Imaging SpectroRadiometer Level 2 Aerosol  
938 Retrieval Algorithm Theoretical Basis, Revision G, JPL D-11400, Jet Propulsion  
939 Laboratory, California Institute of Technology, Pasadena, USA, 2008.
- 940 Eck, T. F., Holben, B.N., Reid, J.S., Dubovik, O., Smirnov, A., O'Neill, N.T., Slutsker, I.,  
941 and Kinne, S., Wavelength dependence of the optical depth of biomass burning, urban,  
942 and desert dust aerosols, *J. Geophys. Res. – Atmos.*, 104, 31333–31349,  
943 doi:10.1029/1999JD900923, 1999.
- 944 Frey, R. A., Ackerman, S. A., Liu, Y., Strabala, K. I., Zhang, H., Key, J. R., & Wang, X.:  
945 Cloud detection with MODIS. Part I: Improvements in the MODIS cloud mask for  
946 collection 5., *J. Atmos. Ocean. Tech.*, 25, 1057-1072, 2008.
- 947 Gupta, P., Levy, R.C., Mattoo, S., Remer, L.A., and Munchak, L.A.: A surface  
948 reflectance scheme for retrieving aerosol optical depth over urban surfaces in MODIS  
949 Dark Target retrieval algorithm, *Atmos Meas Tech*, 9, 3293–3308, doi:10.5194/amt-9-  
950 3293-2016, 2016.
- 951 Gupta, P., Remer, L. A., Levy, R. C., and Mattoo, S.: Validation of MODIS 3 km land  
952 aerosol optical depth from NASA's EOS Terra and Aqua missions, *Atmos. Meas.*  
953 *Tech.*, 11, 3145-3159, <https://doi.org/10.5194/amt-11-3145-2018>, 2018.



- 954 Hsu, N.C., Tsay, S.C., King, M.D. and Herman, J.R.: Aerosol properties over bright-  
955 reflecting source regions. *IEEE Trans. Geosci. Rem. Sens.* 42. 557-569. doi:  
956 10.1109/TGRS.2004.824067, 2004.
- 957 Hsu, N.C., Jeong, M.-J., Bettenhausen, C., Sayer, A.M., Hansell, R., Seftor, C.S., Huang,  
958 J. and Tsay, S.-C.: Enhanced Deep Blue aerosol retrieval algorithm: The second  
959 generation. *J. Geophys. Res. – Atmos.* 118, 9296-9315, doi:10.1002/jgrd.50712, 2013.
- 960 Ichoku, C., Chu, D.A., Mattoo, S., Kaufman, Y.J., Remer, L.A., Tanre, D., Slutsker, I.,  
961 and Holben, B.N., A spatio-temporal approach for global validation and analysis of  
962 MODIS aerosol products, *Geophys Res Lett*, 29, doi:10.1029/2001GL013206, 2002.
- 963 Jickells, T.D., An, Z.S., Andersen, K.K. et al., Global iron connections between desert  
964 dust, ocean biogeochemistry, and climate. *Science*, 308, 67-71, doi:  
965 10.1126/science.1105959, 2005
- 966 Kahn, R. A., Gaitley, B. J., Garay, M. J., Diner, D. J., Eck, T., Smirnov, A., and Holben,  
967 B. N.: Multiangle Imaging SpectroRadiometer global aerosol product assessment by  
968 comparison with the Aerosol Robotic Network, *J. Geophys. Res.*, 115, D23209,  
969 doi:10.1029/2010JD014601, 2010.
- 970 Kahn, R. A., and Gaitley, B.J.: An analysis of global aerosol type as retrieved by MISR.  
971 *J. Geophys. Res. Atmos.*, 120, 4248–4281, doi:10.1002/2015JD02332, 2015.
- 972 Kalashnikova, O.V., and Kahn, R.: Ability of multiangle remote sensing observations to  
973 identify and distinguish mineral dust types: Part 2. Sensitivity over dark water, *J.*  
974 *Geophys. Res. Atmos.*, 111, D11207, doi:10.1029/2005JD00675, 2006.
- 975 Kalluri, S., Alcala, C., Carr, J., Griffith, P., Lebar, W., Lindsey, D., Race, R., Wu, X.,  
976 and Zierk, S.: From photons to pixels: Processing data from the Advance Baseline  
977 Imager, *Remote Sensing*, 10, 10.3390/rs10020177, 2018.
- 978 Kaufman, Y. J., Koren, I., Remer, L. A., Tanré, D., Ginoux, P. and Fan, S.: Dust transport and  
979 deposition observed from the Terra-MODIS spacecraft over the Atlantic Ocean, *J Geophys.*  
980 *Res.*, 110, D10S12, doi:10.1029/2003JD004436,2005
- 981 Koren, I., Kaufman, Y.J., Rosenfeld, D., Remer, L.A. and Rudich, Y.: Aerosol  
982 invigoration and restructuring of Atlantic convective clouds, *Geophys. Res. Lett.*, 32,  
983 L14828, doi: 10.1029/2005GL023187, 2005.



- 984 Levy, R. C., Remer, L.A. and Dubovik, O.: Global aerosol optical properties and  
985 application to Moderate Resolution Imaging Spectroradiometer aerosol retrieval over  
986 land, *J Geophys Res-Atmos*, 112, D13210, doi:10.1029/2006JD007815, 2007a.
- 987 Levy, R. C., Remer, L.A., Mattoo, S., Vermote, E.F. and Kaufman, Y.J.: Second-  
988 generation operational algorithm: Retrieval of aerosol properties over land from  
989 inversion of Moderate Resolution Imaging Spectroradiometer spectral reflectance, *J.*  
990 *Geophys. Res.-Atmos.*, 112, D13211, doi:10.1029/2006JD007811, 2007b.
- 991 Levy, R.C., S. Mattoo, L.A. Munchak, L.A. Remer, A. Sayer, N.C. Hsu. The Collection 6  
992 MODIS aerosol products over land and ocean. *Atmos. Meas. Tech.*, 6, 2989-3034,  
993 2013.
- 994 Levy, R.C., Munchak, L.A., Mattoo, S., Patadia, F., Remer, L.A. and Holz, R.E. :  
995 Towards a long-term global aerosol optical depth record: applying a consistent aerosol  
996 retrieval algorithm to MODIS and VIIRS-observed reflectance. *Atmos. Meas. Tech.*,  
997 8, 4083-4110, <https://doi.org/10.5194/amt-8-4083-2015>, 2015.
- 998 Li, R.-R., Kaufman, Y.J., Gao, B.-C. and Davis, C.O.: Remote sensing of suspended  
999 sediments and shallow coastal waters. *IEEE Trans. Geosci. Remote Sens.*, 41, 559–  
1000 566, 2003.
- 1001 Lim, H., Choi, M., Kim, M., Kim, J., and Chan, P. W.: Retrieval and validation of  
1002 aerosol optical properties using Japanese next generation meteorological satellite,  
1003 Himawari-8. *Korean Journal of Remote Sensing*, 32, 681-691, 2016.
- 1004 Lim, H., Choi, M., Kim, M., Kim, J., Go, S., and Lee, S.: Intercomparing the Aerosol  
1005 Optical Depth Using the Geostationary Satellite Sensors (AHI, GOCI and MI) from  
1006 Yonsei Aerosol Retrieval (YAER) Algorithm. *J. Korean Earth Science Society*, 39,  
1007 119-130, 2018.
- 1008 Lim, H., Choi, M., Kim, J., Kasai, Y., and Chan, P. W.: AHI/Himawari-8 Yonsei Aerosol  
1009 Retrieval (YAER): Algorithm, Validation and Merged Products. *Remote*  
1010 *Sensing*, 10(5), 699, 2018.
- 1011 Lim, S.S., Vos, T., Flaxman, A.D., et al.: A comparative risk assessment of burden of  
1012 disease and injury attributable to 67 risk factors and risk factor clusters in 21 regions,  
1013 1990-2010: a systematic analysis for the Global Burden of Disease Study 2010.  
1014 *Lancet*, 380, 2224-2260, 2012.



- 1015 Lin, J. C., Matsui, T., Pielke Sr., R.A., and Kummerow, C.: Effects of biomass-burning-  
1016 derived aerosols on precipitation and clouds in the Amazon Basin: a satellite-based  
1017 empirical study, *J. Geophys. Res.*, 111, D19204, doi:10.1029/2005JD006884, 2006.
- 1018 Lyapustin, A., Wang, Y., Laszlo, I., Kahn, R., Korkin, S., Remer, L., Levy, R. and Reid,  
1019 J.S.: Multiangle implementation of atmospheric correction (MAIAC): 2. Aerosol  
1020 algorithm. *J. Geophys. Res.* 116, D03211, doi:10.1029/2010JD014986, 2011.
- 1021 Martins, J. V., Tanré, D., Remer, L., Kaufman, Y., Mattoo, S. and Levy, R.: MODIS  
1022 Cloud screening for remote sensing of aerosols over oceans using spatial variability,  
1023 *Geophys Res Lett*, 29, 32139, doi:10.1029/2001GL013252, 2002.
- 1024 Martonchik, J. V., Diner, D. J., Kahn, R., Ackerman, T. P., Verstraete, M. M., Pinty, B.,  
1025 and Gordon, H. R., 1998, Techniques for the retrieval of aerosol properties over land  
1026 and ocean using multiangle imaging, *IEEE Transactions on Geoscience and Remote*  
1027 *Sensing*, 36(4), 1212–1227.
- 1028 Munchak, L. A., Levy, R. C. Mattoo, S., Remer, L.A., Holben, B.N., Schafer, J.S.,  
1029 Hostetler, C.A., and Ferrare, R.A.: MODIS 3 km aerosol product: applications over  
1030 land in an urban/suburban region, *Atmos Meas Tech*, 6, 1747–1759, doi:10.5194/amt-  
1031 6-1747-2013, 2013.
- 1032 Patadia, F., Gupta, P., and Christopher, S. A.: First observational estimates of global clear  
1033 sky shortwave aerosol direct radiative effect over land, *Geophys. Res. Lett.*, 35,  
1034 L04810, <https://doi.org/10.1029/2007GL032314>, 2008.
- 1035 Petrenko, M., Ichoku, C., and Leptoukh, G.: Multi-sensor Aerosol Products Sampling  
1036 System (MAPSS), *Atmos Meas Tech*, 5, 913–926, doi:10.5194/amt-5-913-2012, 2012.
- 1037 Prados, A. I., Kondragunta, S., Ciren, P. and Knapp, K.R.: GOES Aerosol/Smoke  
1038 Product (GASP) over North America: Comparisons to AERONET and MODIS  
1039 observations, *J. Geophys. Res.*, 112, D15201, doi: 10.1029/2006JD007968, 2007.
- 1040 Quaas, J., Ming, Y., Menon, S., Takemura, T., Wang, M., Penner, J. E., and Sayer, A. M.:  
1041 Aerosol indirect effects—general circulation model intercomparison and evaluation  
1042 with satellite data. *Atmos. Chem. Phys.*, 9, 8697–8717, 2009.
- 1043 Remer, L.A., Kaufman, Y.J., Tanré, D., Mattoo, S., Chu, D.A., Martins, J.V., Li, R.,  
1044 Ichoku, C., Levy, R.C., Kleidman, R.G., Eck, T.F., Vermote, E. and Holben,



- 1045 B.N.: The MODIS Aerosol Algorithm, Products, and Validation. *J. Atmos.*  
1046 *Sci.*, 62, 947–973, 2005.
- 1047 Remer, L. A., Mattoo, S., Levy, R.C., Heidinger, A., Pierce, R.B., and Chin, M.:  
1048 Retrieving aerosol in a cloudy environment: aerosol product availability as a function  
1049 of spatial resolution, *Atmos Meas Tech*, 5, 1823–1840, doi:10.5194/amt-5-1823-2012,  
1050 2012.
- 1051 Rosenfeld, D., Sherwood, S., Wood, R. and Donner, L.: Climate effects of aerosol-cloud  
1052 interactions. *Science*, 343, 379-380, DOI: 10.1126/science.1247490, 2014a.
- 1053 Rosenfeld, D., Andreae, A. and Asmi, A.: Global observations of aerosol-cloud-  
1054 precipitation-climate interactions. *Rev. Geophys.* 52, 750–808,  
1055 doi:10.1002/2013RG000441, 2014b.
- 1056 Sekiyama, T. T., Yumimoto, K., Tanaka, T. Y., Nagao, T., Kikuchi, M., & Murakami, H.  
1057 :Data assimilation of Himawari-8 aerosol observations: Asian dust forecast in June  
1058 2015. *Sola*, 12, 86-90, 2016.
- 1059 Seinfeld, John H., et al.: Improving our fundamental understanding of the role of  
1060 aerosol– cloud interactions in the climate system. *Proc. Nat. Acad. Sci.*, 113, 5781-  
1061 5790, 2016.
- 1062 Shi, S., Cheng, T., Gu, X., Letu, H., Guo, H., Chen, H., and Wu, Y.: Synergistic Retrieval  
1063 of Multi-temporal Aerosol Optical Depth over North China Plain Using Geostationary  
1064 Satellite Data of Himawari-8. *Journal of Geophysical Research: Atmospheres*, 123,  
1065 5525–5537. <https://doi.org/10.1029/2017JD027963>.
- 1066 Tanré, D., Herman, M. and Kaufman, Y.: Information on the aerosol size distribution  
1067 contained in the solar reflected spectral radiances, *J. Geophys. Res.*, 101,  
1068 19,043–19,060, 1996.
- 1069 Tanré, D., Kaufman, Y.J., Herman, M., and Mattoo, S.: Remote sensing of aerosol  
1070 properties over oceans using the MODIS/EOS spectral radiances, *J. Geophys. Res.*,  
1071 102, 16,971–16,988, 1997.
- 1072 Tanré, D., Bréon, F. M., Deuzé, J. L., Dubovik, O., Ducos, F., François, P., Goloub, P.,  
1073 Herman, M., Lifermann, A., and Waquet, F. : Remote sensing of aerosols by using  
1074 polarized, directional and spectral measurements within the A-Train: the PARASOL



- 1075 mission, Atmos. Meas. Tech., 4, 1383-1395, <https://doi.org/10.5194/amt-4-1383-2011>,  
1076 2011.
- 1077 Torres, O., Tanskanen, A., Veihelman, B., Ahn, C., Braak, R., Bhartia, P. K., Veeffkind,  
1078 P. and Levelt, P.: Aerosols and surface UV products from OMI observations: An  
1079 overview, J. Geophys. Res., 112, D24S47, doi: 10.1029/2007JD008809, 2007.
- 1080 Torres, O., Ahn, C., and Chen, Z.: Improvements to the OMI near-UV aerosol algorithm  
1081 using A-train CALIOP and AIRS observations. Atmos. Meas. Tech., 6, 3257-3270,  
1082 doi:10.5194/amt-6-3257-2013, 2013.
- 1083 Uesawa, D.: Aerosol Optical Depth product derived from Himawari-8 data for Asian dust  
1084 monitoring, Meteorological Satellite Center Technical Note, No.61, 2016..
- 1085 Wang, J. and Christopher, S. A.: Intercomparison between satellite-derived aerosol  
1086 optical thickness and PM<sub>2.5</sub> mass: Implications for air quality studies. Geophys. Res.  
1087 Lett., 30, 2095, doi:10.1029/2003GL018174, 2003.
- 1088 Yan, X., Li, Z., Luo, N., Shi, W., Zhao, W., Yang, X., and Jin, J.: A minimum albedo  
1089 aerosol retrieval method for the new-generation geostationary meteorological satellite  
1090 Himawari-8, Atmos. Res., 207, 14-27, 2018.
- 1091 Yang, F., Wang, Y., Tao, J., Wang, Z., Fan, M., de Leeuw, G., and Chen, L.: Preliminary  
1092 Investigation of a New AH1 Aerosol Optical Depth (AOD) Retrieval Algorithm and  
1093 Evaluation with Multiple Source AOD Measurements in China, Rem. Sens., 10, 748,  
1094 2018.
- 1095 Yoshida, M., Kikuchi, M., Nagao, T. M., Murakami, H., Nomaki, T., and Higurashi, A.:  
1096 Common retrieval of aerosol properties for imaging satellite sensors, J. Meteorol. Soc.  
1097 Japan. Ser. II, 2018.
- 1098 Yu, F. and Wu, X.: Radiometric Inter-Calibration between Himawari-8 AH1 and S-NPP  
1099 VIIRS for the Solar Reflective Bands, Rem. Sens., 8, 165, 2016.
- 1100 Yu, Hongbin, Remer, L.A., Chin, Mian, Bian, Huisheng, Tan, Qian, Yuan, Tianle and  
1101 Zhang, Yan, Aerosols from overseas rival domestic emissions over North America,  
1102 Science 337, 566-569, doi: 10.1126/science.1217576, 2012.
- 1103 Yu, Hongbin, Remer, L.A., Kahn, R.A., Chin, Mian and Zhang, Yan (2013). Satellite  
1104 perspective of aerosol intercontinental transport: From qualitative tracking to  
1105 quantitative characterization, Atmos. Res. 124, 73-100, doi:



- 1106 10.1016/j.atmosres.2012.12.013, 2013.
- 1107 Yu, H., Chin, M., Yuan, T.L., Bian, H., Remer, L.A., Prospero, J.M., Omar, A., Winker,  
1108 D., Yang, Y.K., Zhang, Y., Zhang, Z. and Zhao, C.: The fertilizing role of African dust  
1109 in the Amazon rainforest: A first multiyear assessment based on data from Cloud-  
1110 Aerosol Lidar and Infrared Pathfinder Satellite Observations, *Geophys. Res. Lett.*, 42,  
1111 1984-1991, doi: 10.1002/2015GL063040, 2015.
- 1112 Yumimoto, K., Nagao, T. M., Kikuchi, M., Sekiyama, T. T., Murakami, H., Tanaka, T.  
1113 Y., and Arai, K.: Aerosol data assimilation using data from Himawari-8, a next-  
1114 generation geostationary meteorological satellite. *Geophys. Res. Lett.*, 43, 5886-5894,  
1115 2016.
- 1116 Zhang, J., Christopher, S.A., Remer, L.A. and YKaufman, Y.J.: Shortwave aerosol  
1117 radiative forcing over cloud-free oceans from Terra: 2. Seasonal and global  
1118 distributions, *J. Geophys. Res.*, 110, D10S24, doi:10.1029/2004JD005009, 2005.
- 1119 Zhang, W., Xu, H., and Zheng, F.: Aerosol Optical Depth Retrieval over East Asia Using  
1120 Himawari-8/AHI Data, *Rem. Sens.*, 10, 137, 2018.
- 1121
- 1122